Geochemistry, Geophysics, Geosystems®

AGU ADVANCING EARTH AND SPACE SCIENCES

RESEARCH ARTICLE
10.1029/2025GC012202

Dual Clumped Isotope (Δ_{47}, Δ_{48}) Values for Calcite Grown at Varying pH and Carbonic Anhydrase Concentrations Constrain Equilibrium and Kinetic Isotope Effects

Jamie Lucarelli[1], Bettina Purgstaller[2], Zeeshan Parvez[1], James M. Watkins[3], Robert A. Eagle[1], Martin Dietzel[2], and Aradhna Tripati[1]

[1]Department of Earth, Planetary, and Space Sciences, Department of Atmospheric and Oceanic Sciences, Institute of the Environment and Sustainability, Center for Diverse Leadership in Science, UCLA, Los Angeles, CA, USA, [2]Institute of Applied Geosciences, Graz University of Technology, Graz, Austria, [3]Department of Earth Science, University of Oregon, Eugene, OR, USA

Abstract This study explores the isotopologues m/z 47 ($^{13}C^{18}O^{16}O$, denoted Δ_{47}) and m/z 48 ($^{12}C^{18}O_2$, denoted Δ_{48}) in CO_2 derived from carbonate minerals, focusing on their temperature dependency, kinetic isotope effects, and distinct reaction pathways. By conducting experiments at four temperatures (5°C, 10°C, 15°C, and 25°C) using the enzyme carbonic anhydrase (CA) at pH 8.3, we approached isotopic equilibrium in dissolved inorganic carbon and measured Δ_{47}, Δ_{48}, and $\delta^{18}O$. Our results were compared with data from Devils Hole cave calcite and existing temperature calibrations, yielding regression equations correlating Δ_{47} and Δ_{48} with temperature: $\Delta_{47\ \text{I-CDES}} = (2.43 \pm 0.289)\ \Delta_{48\ \text{CDES 90}} - (0.006 \pm 0.074)$; $r^2 = 0.96$; $\Delta_{47\ \text{I-CDES}} = (0.038 \pm 0.003) \times 10^6 T^{-2} + (0.161 \pm 0.032)$; $r^2 = 0.99$; $\Delta_{48\ \text{CDES 90}} = (0.015 \pm 0.002) \times 10^6 T^{-2} + (0.076 \pm 0.025)$; $r^2 = 0.94$. Further, calcite precipitated at varying temperatures and pHs of 8.3–11 had kinetic enrichments of Δ_{47} and depletions of Δ_{48} and $\delta^{18}O$ at pH ≥ 9.5, with CA presence leading to distinct kinetic slopes and more efficient Δ_{48} catalysis. These findings are consistent with theoretical predictions for kinetic effects from CO_2 hydration/hydroxylation. Additionally, methodological details for Δ_{48} measurements using the Nu Perspective mass spectrometer are provided, including shot noise calculations, baseline corrections, and how nonlinearity evolves over time. We show that these instruments do not have pressure baseline effects on m/z 48, which is a result of secondary electron suppression on the m/z 48 collector. Therefore, calibration data should be unbiased by these analytical effects.

Plain Language Summary This study explores the complex relationships between clumped isotopes in carbonate minerals and the factors that influence their equilibrium and non-equilibrium states. We conducted controlled experiments using mass 47 and 48 isotopologues of CO_2 formed during the acid digestion of carbonate minerals. Our objective was to understand how temperature and chemical processes affect these isotopologues, specifically focusing on calcite, a common mineral. By precipitating calcite at various temperatures and pH levels, both with and without the enzyme carbonic anhydrase (CA), we examined how these conditions influence isotopic compositions. Our findings highlight the impacts of pH and the presence of CA on isotopic behavior, showing that the enzyme can alter the kinetics of isotope exchange reactions. By comparing our experimental results with theoretical predictions, we attribute some isotopic changes to kinetic effects during CO_2 absorption processes. We also discuss methodological aspects such as noise and baseline corrections in Nu Perspective mass spectrometers.

Key Points:

- Calcite was formed at varying temperatures and pHs, with and without carbonic anhydrase, and examined for equilibrium and kinetics of Δ_{47}, Δ_{48}, and $\delta^{18}O$
- At pH ≥ 9.5, kinetic enrichment in Δ_{47} and depletion in Δ_{48} and $\delta^{18}O$ occur. The presence of CA alters kinetic slopes
- Methodological information for the measurement of Δ_{48} using the Nu Perspective mass spectrometer is discussed

Supporting Information:

Supporting Information may be found in the online version of this article.

Correspondence to:

J. Lucarelli and A. Tripati,
jklucarelli@gmail.com;
atripati@g.ucla.edu

Citation:

Lucarelli, J., Purgstaller, B., Parvez, Z., Watkins, J. M., Eagle, R. A., Dietzel, M., & Tripati, A. (2025). Dual clumped isotope (Δ_{47}, Δ_{48}) values for calcite grown at varying pH and carbonic anhydrase concentrations constrain equilibrium and kinetic isotope effects. *Geochemistry, Geophysics, Geosystems*, *26*, e2025GC012202. https://doi.org/10.1029/2025GC012202

Received 28 JAN 2025
Accepted 9 OCT 2025

1. Introduction

Carbonate clumped isotopes contain two or more rare, heavy isotopes of carbon (^{13}C) or oxygen (^{18}O) within the same molecule. Clumped isotope thermometry is based on the frequency of observation of clumped isotopes in a carbonate mineral compared to a stochastic (random) isotope distribution (Eiler & Schauble, 2004; Ghosh et al., 2006; Schauble et al., 2006; Wang et al., 2004). The dominant clumped isotopologue measured in phosphoric acid digested carbonate minerals is $^{13}C^{18}O^{16}O$, which has a mass of 47 amu (Δ_{47}), while $^{12}C^{18}O^{18}O$ is the dominant mass-48 isotopologue (Δ_{48}). The use of Δ_{47} and Δ_{48} as paleothermometers rely on equilibrium clumped isotope fractionation in the carbonate mineral lattice, and are calculated as

$$\Delta_{47} = (\mathrm{R47}_{\mathrm{sample}}/\mathrm{R47}_{\mathrm{stochastic}} - 1) \times 1000$$

$$\Delta_{48} = (\mathrm{R48}_{\mathrm{sample}}/\mathrm{R48}_{\mathrm{stochastic}} - 1) \times 1000$$

where Ri_{sample} is the measured ratio of i/44 CO_2 isotopologues in the sample, and $Ri_{\mathrm{stochastic}}$ is the ratio of i/44 CO_2 isotopologues at a stochastic distribution (Eiler & Schauble, 2004; Ghosh et al., 2006; Schauble et al., 2006; Wang et al., 2004).

However, theoretical and experimental work has shown that some biogenic and abiogenic carbonate minerals yield disequilibrium Δ_{47} (Daëron et al., 2011; Daeron et al., 2019; Ghosh et al., 2006; Guo et al., 2019; Saenger et al., 2012; Tang et al., 2014; Tripati et al., 2015) and Δ_{48} values (Bajnai et al., 2020; Davies et al., 2022, 2023; Fiebig et al., 2021; Guo, 2020; Lucarelli, Carroll, et al., 2023; Lucarelli, Purgstaller, et al., 2023; Parvez et al., 2023, 2024; Staudigel et al., 2023; Tagliavento et al., 2023; Tripati et al., 2015). Disequilibrium Δ_{47} can be correlated with $\delta^{18}O$ disequilibria and observed in experiments at elevated pH (e.g., Tang et al., 2014). Multiple marine calcifier species, including scleractinian corals, are known to significantly elevate the pH of their calcifying fluid which may influence mineral isotopic compositions (Adkins et al., 2003; Al-Horani et al., 2003; Anagnostou et al., 2012; Bajnai et al., 2020; Eagle et al., 2022; Kimball et al., 2016; Liu et al., 2020; Saenger et al., 2012; Spooner et al., 2016; Trotter et al., 2011; Venn et al., 2011, 2025). Additionally, strongly alkaline abiotic carbonate precipitation occurs in surface and subsurface aqueous systems, such as alkaline springs with pH > 11 (Christensen et al., 2021; Parvez et al., 2023).

Multiple mechanisms have been proposed to explain disequilibrium Δ_{47} values in carbonate minerals. Clumped isotopic disequilibrium can arise from mineral growth from an equilibrated dissolved inorganic carbon (DIC) pool from speciation effects (e.g., Hill et al., 2014, 2020; Tripati et al., 2015; Watkins & Hunt, 2015). Carbonate mineral precipitation can occur before isotopic equilibration of DIC (Beck et al., 2005; Staudigel & Swart, 2018; Tripati et al., 2015). CO_2 hydration and hydroxylation reactions are another potential source of isotopic disequilibrium (Bajnai et al., 2020; Boettger & Kubicki, 2021; Guo, 2020; Parvez et al., 2023; Staudigel & Swart, 2018), as are dehydration and dehydroxylation reactions, and these can arise from CO_2 absorption and degassing processes (Daeron et al., 2011; Guo, 2020; Parvez et al., 2024). Aqueous ion and CO_2 gas diffusion (Thiagarajan et al., 2011), and organism-specific vital effects from enzymatic activity and metabolism have also been hypothesized to give rise to clumped isotope disequilibrium (Davies et al., 2022; Spooner et al., 2016). Clumped isotopic disequilibrium in the DIC pool has been hypothesized to be modulated by carbonate precipitation rate (Tripati et al., 2015), oxygen isotopes in water (Dietzel et al., 2009; Watkins et al., 2014), and carbon and oxygen isotope exchange between water and the atmosphere (Parvez et al., 2024).

CO_2 hydration (Reaction 1) and hydroxylation (Reaction 2) reactions are responsible for $^{18}O/^{16}O$ equilibration, as they are the only direct route for the exchange of O atoms between H_2O and DIC (Zeebe & Wolf-Gladrow, 2001). Clumped and oxygen isotope equilibration of DIC and carbonate minerals are also controlled by 5 additional key reactions (Reactions 3–7) (Guo, 2020; Watkins and Devriendt, 2022).

$$CO_2 + H_2O \leftrightharpoons HCO_3^- + H^+ \quad \text{(R1)}$$

$$CO_2 + OH^- \leftrightharpoons HCO_3^- \quad \text{(R2)}$$

$$HCO_3^- \leftrightharpoons CO_3^{2-} + H^+ \quad \text{(R3)}$$

$$HCO_3^- + OH^- \leftrightharpoons CO_3^{2-} + H_2O \quad \text{(R4)}$$

$$H_2O \leftrightharpoons H^+ + OH \quad \text{(R5)}$$

$$Ca^{2+} + HCO_3^- \leftrightharpoons CaCO_3 + H^+ \quad \text{(R6)}$$

$$Ca^{2+} + CO_3^{2-} \leftrightharpoons CaCO_3 \quad \text{(R7)}$$

Equilibrium isotopic compositions are obtained when DIC and H_2O have had sufficient time to isotopically equilibrate, and mineral precipitation is slow. When DIC and H_2O have not been equilibrated or precipitation is rapid, kinetic isotope effects (KIEs) and disequilibrium isotopic compositions can be recorded in a forming carbonate mineral. The time to reach isotopic equilibrium is governed by the forward and reverse CO_2 hydration and hydroxylation rate constants, which depend on temperature (Zeebe & Wolf-Gladrow, 2001), and DIC speciation, which is a function of temperature and pH (Tripati et al., 2015; Uchikawa & Zeebe, 2012). The rate constant for hydration is not sensitive to ionic strength (Johnson, 1982; Knocke, 1980; Miller et al., 1971; Zeebe & Wolf-Gladrow, 2001), whereas a subtle dependency has been documented for the hydroxylation rate constant (Johnson, 1982). Higher temperature results in faster reaction kinetics and thus faster isotopic equilibration of the DIC pool. A higher pH causes much longer isotopic equilibration times induced by low molar fraction of aqueous CO_2 in DIC, leading CO_2 to be mostly unavailable for isotope exchange in Reactions 1 and 2 (Beck et al., 2005; Weise & Kluge, 2020). For example, at 25°C at pH 8.7, ^{18}O equilibration is reached at ∼17 hr, whereas at pH 12, ^{18}O equilibration is reached at ∼35 days (Beck et al., 2005). At 40°C and a pH of 12, ^{18}O equilibration time is reduced to ∼10 days (Beck et al., 2005).

The addition of the enzyme carbonic anhydrase (CA) catalyzes the forward and reverse hydration reaction and thus significantly decreases the time to reach isotopic equilibrium. The uncatalyzed hydration reaction rate at 25°C and pH 7.4 is $\sim 10^{-1}$ s^{-1}, while the CA catalyzed rate can reach $\sim 10^{6}$ s^{-1} depending on [CA] (Kernohan, 1964), where highest catalyzation effects are achieved at pH > 8 (Berg et al., 2002). Many marine calcifiers used for climate reconstructions are thought to have CA within their calcifying space, including coccolithophores (Nimer et al., 1994; Soto et al., 2006) and other phytoplankton (Rost et al., 2003), oysters (Miyamoto et al., 1996; Yu et al., 2006), coral (Al-Horani et al., 2003; Bertucci et al., 2011; Kurman et al., 2017; Moya et al., 2008; Weis et al., 1989), and benthic foraminifera (de Goeyse et al., 2019). Clumped isotope measurements support the activity of CA in the calcifying fluid of warm water corals (Davies et al., 2022). However, the role that CA plays in calcification is not completely known, including the effectiveness of CA in reducing clumped and bulk KIEs at high pH and varying temperatures.

When carbonate minerals precipitate under clumped isotopic disequilibrium, this may result in an over- or underestimation of the reconstructed temperature. However, the dual measurement of Δ_{47} and Δ_{48} has been theoretically (Guo, 2020; Hill et al., 2014, 2020; Tripati et al., 2015) and experimentally (Bajnai et al., 2020; Fiebig et al., 2019, 2021; Lucarelli, Carroll, et al., 2023; Swart et al., 2021) shown to have a characteristic equilibrium relationship. The equilibrium Δ_{47}-Δ_{48} relationship along with constrained boundaries of disequilibrium trajectories in DIC and carbonate minerals may be used to identify the origin of KIEs (Bajnai et al., 2020; Davies et al., 2022, 2023; Guo, 2020; Lucarelli, Purgstaller, et al., 2023; Parvez et al., 2023, 2024). It may be possible to correct for KIEs and recover equilibrium clumped isotope values from samples (Bajnai et al., 2020; Davies et al., 2023; Guo, 2020).

Through comparison of experimental data with theoretical predictions, a robust framework can be developed to advance the dual carbonate clumped isotope approach as a potential tool for constraining KIEs, including vital effects in biogenic carbonates. Currently, the Δ_{47}-Δ_{48} trajectory of KIEs in carbonate minerals is limited to theory with calculations for a DIC pool at equilibrium (Hill et al., 2014; Tripati et al., 2015), hydration/hydroxylation (Guo, 2020), carbonate minerals from peridotite associated springs (Parvez et al., 2023), and for growth from a solution of DIC with cations present (Hill et al., 2020). Theory has been used to explain some measurements of disequilibrium Δ_{47}-Δ_{48} values in speleothems, stalagmites, corals, brachiopods and high magnesium calcite formed from amorphous precursors (Bajnai et al., 2020; Davies et al., 2022, 2023; Guo, 2020; Lucarelli, Purgstaller, et al., 2023; Parvez et al., 2023, 2024; Tagliavento et al., 2023).

Here, we adapted experimental approaches used in Tang et al. (2014) and Tripati et al. (2015) to constrain KIEs in Δ_{47}, Δ_{48}, and $\delta^{18}O$ in calcite precipitated under controlled conditions at different pHs and temperatures (T), with and without the addition of CA. We compared data from calcite grown under isotopic disequilibrium conditions at varying pH to calcite formed at quasi-equilibrium conditions. We aim to further constrain equilibrium and kinetically governed relationships for clumped isotopes, including Δ_{47}-Δ_{48}, Δ_{47}-T, Δ_{48}-T, Δ_{47}-$\delta^{18}O$ and Δ_{48}-$\delta^{18}O$. Our experimental results were compared to model calculations.

2. Methods

2.1. Calcite Precipitation Experiments

Calcite was precipitated under controlled conditions at pH 8.3, 9.0, 9.5, 10.0, 10.5, and 11.0 at 5°C, 10°C, 15°C, and 25°C, with and without the addition of CA (molecular weight 29,000 g/mol). CA has been shown to be active in catalyzing CO_2 hydration at all pH values used in our experiment (Kernohan, 1964). Experimental conditions are given in Table 1. Calcite was precipitated using a method adapted from Dietzel et al. (2004). A schematic of the precipitation apparatus is shown in Figure 1. In all experiments, a 0.5 L bottle composed of 2 mm thick polyethylene was filled with 0.83 M $NaHCO_3$ and 2 M HCl and placed inside a 5 L outer container filled with 4.9 L Milli Q water, 10 mM $CaCl_2$, 0.01 mM $SrCl_2$, 50 mM NaCl, and no DIC. All chemicals were of reagent grade from Merck.

The pCO_2 gradient between the inner and outer containers caused CO_2 gas to diffuse through the polyethylene membrane into the outer container solution where the CO_2 reacted to form carbonate ions that precipitated as $CaCO_3$. The outer solution was constantly stirred with a large floating stir bar by placing the containers on top of a stir plate at 200 rpm. A piece of Styrofoam was placed between the stir plate and solution to prevent temperature changes. The pH of the outer container solution was held constant by a Schott TitroLine alpha plus titrator (±0.03 accuracy) with 2 M NaOH. The entire precipitation apparatus was placed inside an Aqualytic Thermostatic Cabinet (±0.5°C accuracy) to hold the precipitation temperature constant. In experiments with CA, 0.25 μM CA was added to the outer solution. A concentration of 0.25 μM CA should be sufficient to maintain oxygen isotopic equilibrium among DIC species up to at least pH 9.3 (Watkins et al., 2014). Each experiment yielded 30–40 mg of precipitate. The mineralogy of the precipitate was determined using an X-ray powder diffraction (XRD) PANalytical X'Pert PRO diffractometer (see Data Availability Statement). The mineral phase was determined using PANalytical X'Pert HighSchore Plus software.

Every 2–3 days, a 2 ml sample of the solution was removed from the outer solution via a syringe that was inserted into an airtight port through the lid of the apparatus. The solution was filtered through a 0.2 μm cellulose acetate membrane to remove any precipitate and subsequently analyzed for trace elements on a Perkin Elmer Optime 4300DV Inductively Coupled Plasma—Optical Emission Spectrometer (ICP-OES). This analysis yielded the [Ca], allowing for the estimation of the precipitation rate by $([Ca]_{final} - [Ca]_{initial})/(t_{final} - t_{initial})$, which was converted to mol m^{-2} s^{-1} using a specific surface area of 0.27 m^2/g (Tang et al., 2008). Oxygen isotopes of the precipitation solution were measured at the start and end of most experiments by wavelength-scanned cavity ring-down spectroscopy (WS-CRDS) using a Picarro L2140-i system. Typical analytical precision (1 σ) was ±0.05‰ for $\delta^{18}O_{water}$, where the values are referenced relative to the Vienna Standard Mean Ocean Water (VSMOW).

2.2. Mass Spectrometry

2.2.1. Instrumentation

Standards and samples were analyzed on three isotope ratio mass spectrometers (IRMS) in the Eagle-Tripati Laboratory during 2018–2021. The instruments used in this work were a Thermo Fisher MAT 253, and two Nu Instruments Perspective mass spectrometers, with both Nu Instruments having multiple configurations (Table 2). Only data from the Nu Instruments were used in Δ_{48} analyses. The instrumental configurations used here have been shown through data comparisons and statistical analysis to yield equilibrium Δ_{47} and Δ_{48} values, and standard values, which are comparable to data reported by other groups (Defliese & Tripati, 2020; Lucarelli, Carroll, et al., 2023; Upadhyay et al., 2021). A typical daily run on all instruments consists of an equal number of samples and standards, with standards bracketing the samples. Raw data were processed and corrected in the Easotope 64-bit version from release 20201231 (John & Bowen, 2016) using the IUPAC parameter set (Brand et al., 2010; Daëron et al., 2016).

The Thermo Fisher MAT 253 (not used for Δ_{48} measurements) used an autosampler similar to what is described in Passey et al. (2010) with a 105 weight % phosphoric acid bath held at 90°C. After 5 mg calcite samples were digested, CO_2 (g) was cryogenically purified through traps containing dry ice-cooled ethanol and liquid nitrogen, which remove low vapor pressure gases such as H_2O (g). CO_2 passed through elemental silver wool (Sigma Aldrich), followed by a −20°C gas chromatograph (GC) that contained Porapak Type-Q™ 50/80 mesh column pack material with He carrier gas. The detectors for *m/z* 44, 45, and 46 are registered through 3×10^8, 3×10^{10}, and 10^{11} Ω resistors, respectively, while *m/z* 47–49 are registered through 10^{12} Ω resistors. Data are acquired in

Table 1
Experimental Conditions for Precipitation Experiments

Temperature of precipitation (°C)	pH of precipitation solution	CA (yes or no)	Time from beginning of experiment until start of precipitation (days)	Total experiment time (days)	Precipitation rate $\log_{10}R$ (mol m^{-2} s^{-1})	Initial water $\delta^{18}O_{VSMOW}$ (‰)	Final water $\delta^{18}O_{VSMOW}$ (‰)	Calcite (weight %)	Vaterite (weight %)	Aragonite (weight %)
5	8.3	Y	23	34	−7.11	n/a	−9.52	100		
5	8.3	N	29	52	−7.43	n/a	−9.44	100		
5	9.0	Y	3	27	−7.45	−9.22	−9.14	100		
5	9.0	N	5	27	−7.41	−9.40	−9.31	100		
5	9.5	Y	1	26	−7.47	−9.37	−9.26	100		
5	9.5	N	<1	26	−7.48	−9.44	−9.33	100		
5	10.0	Y	<1	9	−7.02	−9.47	−9.13	100		
5	10.0	N	<1	9	−7.02	−9.64	−9.56	100		
5	10.5	Y	<1	14	−7.21	n/a	−9.07	100		
5	10.5	N	<1	14	−7.21	−9.37	−9.25	100		
5	11.0	Y	<1	12	−7.15	n/a	−9.44	100		
5	11.0	N	<1	12	−7.15	n/a	n/a	100		
10	8.3	Y	14	26	−7.15	−9.26	−9.40	100		
10	8.3	N	10	26	−7.27	−9.18	−9.35	100		
10	10.5	Y	1	15	−7.21	−8.83	−8.86	21	75	4
10	10.5	N	1	15	−7.21	−8.96	−9.01	100		
15	8.3	Y	9	20	−7.11	−9.03	−9.15	100		
15	8.3	N	9	20	−7.11	−9.16	−9.10	100		
15	10.5	Y	<1	14	−7.21	−9.22	−9.02	54	43	3
15	10.5	N	<1	14	−7.21	−9.34	−9.06	100		
25	8.3	Y	2	14	−7.15	−9.30	−9.29	100		
25	8.3	N	3	14	−7.11	−9.32	−9.33	100		
25	10.5	Y	<1	12	−7.15	−9.53	−9.38	72	2	26
25	10.5	N	<1	12	−7.15	−9.33	−9.29	60		40

Note. Mineralogy was determined by XRD.

nine blocks of 10 cycles, with each consisting of 8 s of integration and 16 s of changeover delay, for a total integration time of 720 s.

We used two Nu Perspective isotope ratio mass spectrometers to determine Δ_{47} and Δ_{48} values. The detectors for *m/z* 44, 45, and 46 are registered through 3×10^8, 3×10^{10}, and 10^{11} Ω resistors, respectively. The detectors for *m/z* 47–49 are registered through 10^{12} Ω resistors. A secondary electron suppressor (miniature electrostatic analyzer) with a negative potential (−50 V) is in front of each Faraday collector, which prevents secondary electrons produced when analyte ions impact the base of the collector from escaping. Each suppressor has a ground plate in front and behind it. The suppressors also prevent low energy electrons produced when stray ions collide with internal surfaces from entering a collector. Additionally, there is a "mop plate" located before the suppressors, which has a positive voltage (+50 V). The mop plate repels ions that are outside the normal ion path and attracts low energy electrons to prevent them from entering the collectors.

Nu Perspective-1a, -1b, and -1c are the same mass spectrometer with different sampling methods (Table 2). Nu Perspective-1a used the same autosampler setup as the MAT 253 containing 1–2 mg samples, an acid digestion temperature of 90°C, common acid bath, GC, He carrier gas, and cryogenic purification traps. Nu Perspective-1b used 0.5 mg samples, a 70°C acid digestion temperature in individual glass vials, and a shorter GC column called an adsorption trap that is under vacuum (no carrier gas), which contains Poropak Type Q™. Nu Perspective-1c used an acid digestion temperature of 90°C in a common acid bath, 0.5 mg samples, and an adsorption trap. Nu

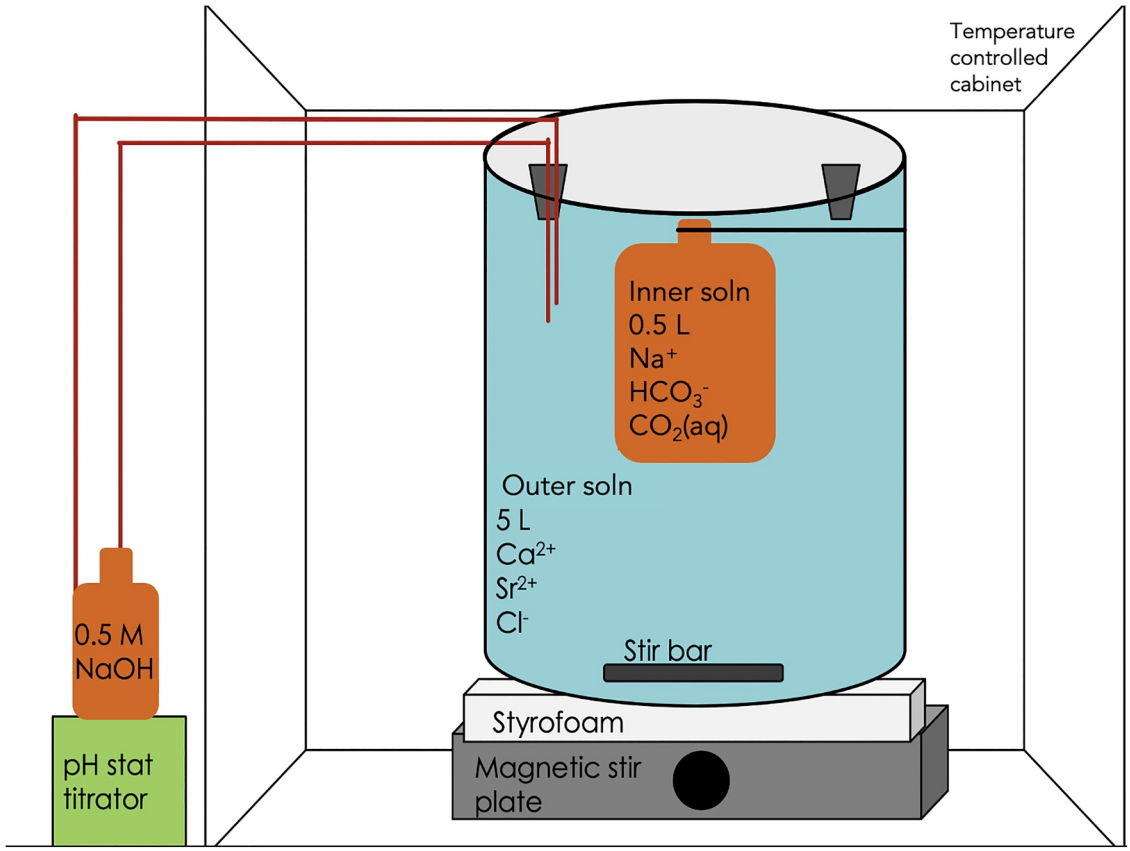

Figure 1. Schematic of the precipitation apparatus used for this work. The inner bottle is a 0.5 L, 2 mm thick polyethylene bottle that serves as a membrane through which CO_2 diffuses into the outer solution. The outer solution is inside a 5 L container that contains Ca^{2+} from CaCl. A pH-stat titrator holds the pH of the outer solution constant by titrating NaOH. The temperature is held constant by placing the entire apparatus inside a temperature-controlled cabinet. The apparatus was adapted from Dietzel and Usdowski (1996), Dietzel et al. (2004), Tang et al. (2008), and Tang et al. (2014).

Perspective-2a and -2b are the same mass spectrometer with different sampling methods (Table 2). Nu Perspective-2a used 70°C acid digestion, individual glass sample vials, and an adsorption trap. Nu Perspective-2b used a 90°C acid digestion temperature, common acid bath, and adsorption trap. Both configurations used 0.5 mg samples. All samples were analyzed in microvolume mode where the sample and working gas have matched volumes that are depleted at the same rate.

Sample and standard measurements on the Nu Perspectives were taken in 3 acquisition blocks of 20 cycles. Each cycle consists of 20 s of integration and 8 s of changeover delay, yielding a total integration time of 1,200 s. The

Table 2
Mass Spectrometer Configurations Used in This Study

Mass spectrometer	Acid digestion T (°C)	Acid digestion method	Sample size (mg)	GC column with He carrier gas	Adsorption trap	m/z 44 ion beam intensity (V)	Integration time (s)	Δ_{47} shot noise limit (‰)	Δ_{48} shot noise limit (‰)
Thermo Fisher MAT 253	90	Common acid bath	5	x		16	720	0.013	
Nu Perspective-1a	90	Common acid bath	1–2	x		18	1,200	0.010	0.032
Nu Perspective-1b	70	Individual vials	0.5		x	24-9	1,200	0.008–0.013	0.027–0.044
Nu Perspective-1c	90	Common acid bath	0.5		x	24-9	1,200	0.008–0.013	0.027–0.044
Nu Perspective-2a	70	Individual vials	0.5		x	24-9	1,200	0.008–0.013	0.027–0.044
Nu Perspective-2b	90	Common acid bath	0.5		x	24-9	1,200	0.008–0.013	0.027–0.044

repeatability of m/z 48 on an acquisition level (3 acquisitions per measurement) was examined by plotting the difference between the $\Delta_{48\ raw}$ value for each acquisition and the $\Delta_{48\ raw}$ value for the measurement ($\Delta\Delta_{48\ raw}$) versus the difference between the m/z 44 for the sample and reference gas (Figure S1 in Supporting Information S1). The $\Delta\Delta_{48\ raw}$ value through time was also examined (Figure S1 in Supporting Information S1). For Nu Perspective-1, only 13 acquisitions out of 1,502 fell outside of the 3 SD threshold. For Nu Perspective-2, 18 acquisitions out of 2,487 fell outside of the 3 SD threshold. For both instruments, the acquisitions with higher error occurred when the instruments were restarted after a source replacement (Nu Perspective-1) and repair (Nu Perspective-2). The Δ_{47} and Δ_{48} shot noise limits (1 SD) for the Nu Perspective configurations used here range from 0.008–0.013‰ to 0.027–0.032‰, respectively, calculated using equations from Merritt and Hayes (1994), Huntington et al. (2009), and Petersen and Shrag (2014). The average external error (SE and SD for replicate analyses) for the samples reported here was as follows: Δ_{47} 1 SE = 0.008‰ and 1 SD = 0.022‰; Δ_{48} 1 SE = 0.022‰ and 1 SD = 0.056‰. The average internal error (SE and SD for acquisitions in each replicate) for the samples in this study was as follows: $\Delta_{47\ raw}$ 1 SE = 0.013‰ and 1 SD = 0.023‰; $\Delta_{48\ raw}$ 1 SE = 0.044‰ and 1 SD = 0.076‰. The average internal error for the standards in this study was as follows: $\Delta_{47\ raw}$ 1 SE = 0.013‰ and 1 SD = 0.024‰; $\Delta_{48\ raw}$ 1 SE = 0.045‰ and 1 SD = 0.078‰. Overall, the SE values for internal and external error were consistent with shot noise, except for the SE for $\Delta_{48\ raw}$, which was 0.012‰ and 0.013‰ higher than shot noise for samples and standards, respectively. All external and internal errors are reported in Tables S1–S5 (see Data Availability Statement). The fully propagated sample error reported in tables and figures was calculated manually using Equation 11 from Daëron (2021) where

$$\sigma\left(\overline{\Delta_{47}}\right)^2 = \sigma_u^2 + \sigma_s^2$$

$$\sigma_u^2 = \sigma_{47}^2/N_a$$

$$\sigma_s^2 = \frac{\sigma_{47}^2}{N}.$$

Manual calculation was necessary because the other reported methods in Daëron (2021) do not account for a moving standardization window.

2.2.2. Data Corrections

On the Nu Instruments, a blank measurement (no gas in the source) is taken at the beginning of each block (3 total blocks) of sample and reference gas data. The blank value is subtracted from the sample and reference gas measurements to give blank corrected values. This results in an intensity measurement referenced to a baseline of ~0 mV. This is illustrated by the blank scans for m/z 44–49 and peak scans for mass 48 in Figure S2 of Supporting Information S1. A blank correction is also performed for the MAT 253. However, the Nu Instruments initially report data in raw replacement current, which is converted to intensity, whereas on the MAT 253, the data are converted in the instrument control software and are reported directly in intensity.

The data then undergo a nonlinearity correction determined using the standards ETH-1 and ETH- 2 (Bernasconi et al., 2018, 2021). The nonlinearity correction is followed by scale compression/stretching using an empirical transfer function (ETF), using methods detailed in Dennis et al. (2011). The nonlinearity and ETF corrections are calculated from a moving window of ±10 standard replicates (20 total), similar to Meckler et al. (2014), Upadhyay et al. (2021), Griffiths et al. (2023), and Lucarelli, Carroll, et al. (2023). Due to the use of a moving correction window, the nonlinearity and ETF slopes used in data corrections fluctuate, but the average ETF and nonlinearity slopes for each instrument are similar to what is reported by other laboratories (Δ_{47}, Δ_{48} ETF slope = ~1; Δ_{47} nonlinearity slope = 0.00001–0.001; Δ_{48} nonlinearity slope = 0.001–0.01) that use corrections based on the average of a whole interval. The use of a moving correction window accounts for within-interval drift. We note that other groups that use whole-interval corrections account for within-interval drift using fourth order polynomials (e.g., Bernecker et al., 2023; Fiebig et al., 2021). Figure S3 in Supporting Information S1 reports Δ_{47raw} versus δ^{47} and $\Delta_{48\ raw}$ versus δ^{48} for ETH-1 and ETH-2 standards used in nonlinearity corrections, and Figure S4 in Supporting Information S1 shows the variation of the nonlinearity correction over time. Figure S5 in Supporting Information S1 shows the slopes and intercepts used in ETFs. No acid fractionation

factors were used. The samples analyzed at 70°C were transformed into the 90°C reference frame using ETFs based on standards analyzed at 90°C, similar to Bernasconi et al. (2021).

The Δ_{47} data are presented relative to international standards ETH-1, ETH-2, and ETH-3 (Bernasconi et al., 2018, 2021), and the in-house carbonate standards, Veinstrom and Carrara Marble Tile (CM Tile) (Lucarelli, Carroll, et al., 2023; Upadhyay et al., 2021), in the I-CDES reference frame (Bernasconi et al., 2021) at 90°C, $\Delta_{47\ \text{I-CDES}}$. The Δ_{48} data are presented relative to the same carbonate standards in the 90°C reference frame, $\Delta_{48\ \text{CDES 90}}$. The Δ_{48} values used in transfer functions are based on long-term average values from our laboratory of 0.132 ± 0.003‰ for ETH-1 (n = 464), 0.132 ± 0.003‰ for ETH-2 (n = 439), 0.247 ± 0.004‰ for ETH-3 (n = 236), 0.145 ± 0.003‰ for CM Tile (n = 309), and 0.273 ± 0.003‰ for Veinstrom (n = 436) (Lucarelli, Carroll, et al., 2023). We used the 3σ (σ = 1 SD) outlier exclusion method for standard and sample data, similar to what is reported in Meckler et al. (2014), Parvez et al. (2023), and Lucarelli, Carroll, et al. (2023). For the data collection windows included in this work, an average of 5% of Δ_{47} standards and 11% of Δ_{48} standards were disabled in Eastotope, meaning their values were not used in corrections. All standard and sample replicate data are reported in Tables S1–S5 (see the Data Availability Statement).

2.3. Converting Δ_{47} and Δ_{48} to Δ_{63} and Δ_{64}

Measured Δ_{47} and Δ_{48} values were converted to theoretical calcite mineral Δ_{63} and Δ_{64}, respectively, for direct comparison to model predictions for kinetic and equilibrium relationships in calcite. This conversion was carried out using compositionally dependent acid fractionation factors (AFFs), $\Delta^*_{63\text{-}47}$ and $\Delta^*_{64\text{-}48}$, from Lucarelli, Carroll, et al. (2023) (Equations 1–4).

$$\Delta^*_{63\text{-}47} = 0.0190 \times \Delta_{47\ \text{I-CDES}} + 0.1842 \quad (1)$$

$$\Delta^*_{64\text{-}48} = 0.0077 \times \Delta_{48\ \text{CDES 90}} + 0.1290 \quad (2)$$

$$\Delta_{63} = \Delta_{47\ \text{I-CDES}} - \Delta^*_{63\text{-}47} \quad (3)$$

$$\Delta_{64} = \Delta_{48\ \text{CDES 90}} - \Delta^*_{64\text{-}48} \quad (4)$$

2.4. Parameters Used for IsoDIC Modeling

The IsoDIC model (Guo, 2020) was used to estimate the isotopic evolution of HCO_3^- and CO_3^{2-} end-members during CO_2 absorption in an aqueous solution at pH 10.5, under conditions similar to our experiments. This numerical modeling software predicts kinetic clumped isotope fractionations in the DIC-H_2O-CO_2 system. The model simulates five key reactions (Reactions 1–5) that control isotope fractionation, and all related isotopologue reactions involving ^{12}C, ^{13}C, ^{16}O, ^{17}O, and ^{18}O, for a total of 155 reactions. The forward and reverse rate constants were estimated using Equation 5,

$$k^* = \alpha_{\text{KIE}} \times k \quad (5)$$

where k^* is the rate constant of the isotopically substituted reaction, k is the rate constant of the isotopically non-substituted reaction, and α_{KIE} is the kinetic isotope fractionation factor for the isotopically substituted reaction. Isotopic equilibrium was assumed between HCO_3^- and CO_3^{2-} and H_2O and OH^- due to rapid equilibration via Reactions 3–5 relative to the reaction rate of hydration (Reaction 1) and hydroxylation (Reaction 2). Therefore, the only reactions that contribute to isotopic fractionation in the IsoDIC model are the forward and reverse CO_2 hydration and hydroxylation reactions (Guo, 2020).

To use the IsoDIC model in the CO_2 absorption regime, we assumed the model default values for $\delta^{13}C$ of the CO_2 in air to be −10‰, $\delta^{18}O_{\text{VSMOW}}$ of water to be 0‰, and $\Delta'^{17}O_{\text{VSMOW}}$ of water to be 0‰ (Guo, 2020). The initial oxygen and clumped isotope values of DIC and air were set to be in equilibrium with water. We set the solution temperature to be 5°C in the first simulation and 25°C in the second simulation, both with a solution pH of 10.5. The model has a total evolution time of 12 hr. The full set of equations used is available in Guo (2020).

2.5. Box Model for Kinetic Isotope Effects in Δ_{47}, Δ_{48}, and $\delta^{18}O$

To predict KIEs in calcite during CO_2 absorption for Δ_{47}, Δ_{48}, and $\delta^{18}O$, we used a box model that tracks the carbon, oxygen, and clumped isotopic composition of DIC species in a homogeneous (i.e., well-stirred) CO_2-fed solution built on the ExClump38 framework (Chen et al., 2018; Uchikawa et al., 2021; Watkins and Devriendt, 2022). In the model, the CO_2 influx is counter-balanced by a $CaCO_3$ outflux that is based on precipitation from Reactions 6 and 7. Mineral precipitation affects the isotopic composition of DIC in two ways: (a) the rate constants for Reactions 6 and 7 are mass dependent and can therefore influence the isotopic composition of residual DIC (Watkins & Hunt, 2015) and (b) the rate of calcite precipitation affects the degree of hydration/hydroxylation reaction reversibility at steady state and the extent to which the KIEs attending these reactions are expressed in solution.

In the model, we set $[Ca^{2+}] = 10$ mM and added enough DIC to bring the initial degree of supersaturation to 7 (Equation 6), as estimated from Dietzel et al. (2009) for spontaneous nucleation of calcite,

$$\Omega = \frac{\left[CO_3^{2-}\right]\left[Ca^{2+}\right]}{K_{sp\ (calcite)}} \sim 7 \tag{6}$$

where Ω is the saturation state and K_{sp} is the solubility product for calcite. The DIC is initially isotopically equilibrated. As CO_2 fluxes into solution, it gets converted to isotopically lighter-than-equilibrium HCO_3^- and CO_3^{2-} by hydration (Reaction 1) and hydroxylation (Reaction 2). The rate of calcite growth depends on $[Ca^{2+}]$ and $[CO_3^{2-}]$, which is updated at each time step. Each simulated experiment lasts 1,000 hr, which is far longer than the time required to reach steady state, and outputs the steady state composition of each DIC species and calcite. We treat the equilibrium and kinetic fractionation factors as "known" and adopt the previous estimate for the representative total reactive surface area of calcite in these experiments (0.01 m^2; Watkins & Devriendt, 2022). We vary the temperature (T), pH, flux of CO_2 (F_{CO2}), and [CA], and assess how well the model predicts the trends observed in the data. A description of all equations and parameters used are provided in Supporting Information S1 (Section S.2). Further information about the model can be found in Watkins and Devriendt (2022).

We report the steady state Δ_{47}, Δ_{48}, $\delta^{13}C$, and oxygen isotope fractionation factor ($\alpha_{calcite-water}$) at variable pH from 8.3 to 11, at temperatures of 5 and 25°C, and variable F_{CO2} (related to calcite growth rate) ranging from typical experimental rates to those from extremely slow calcite growth.

We repeated the same model calculations but simulated the impact of the addition of 0.25 μM CA. All model calculations had 0‰ salinity, while experiments had a starting ionic strength of ~0.045 mol/L. This should have a negligible effect on our model calculations given that the reaction rate constants will not be affected by the ionic strength. We compared the results of the model calculations (with and without CA) to our experimental data (with and without CA) and to experimental data from precipitation experiments reported in Tang et al. (2014).

3. Results

3.1. Calcite Precipitated With and Without Carbonic Anhydrase

3.1.1. $\delta^{13}C$ and $\delta^{18}O$

Calcite, verified by XRD (see Data Availability Statement), had a negative correlation between pH and $\delta^{18}O$ (Figures 2a–2d, Table 3). The largest $\delta^{18}O$ depletion relative to the quasi-equilibrium sample (precipitated at the same temperature at pH 8.3 with CA) was observed in samples with the lowest temperature and highest pHs. The samples formed at 5°C and pHs of 10.5 and 11.0 had $\delta^{18}O$ depletions of 17.7‰ and 18.8‰, respectively. All samples precipitated with and without CA at pH 8.3 had statistically identical $\delta^{18}O$ values. At 5°C, depletions in $\delta^{18}O$ were observed at pH ≥ 9. Calcite precipitated without CA had depleted $\delta^{13}C$ when compared to samples precipitated with CA for all temperatures and pHs (Figures 2e–2h, Table 3).

3.1.2. Δ_{47} and Δ_{48}

For a given temperature, calcite precipitated with and without CA at pH 8.3 had statistically identical Δ_{47} and Δ_{48}. Samples precipitated without CA at pH ≥ 9.5 had enriched Δ_{47} and depleted Δ_{48} values relative to calcite

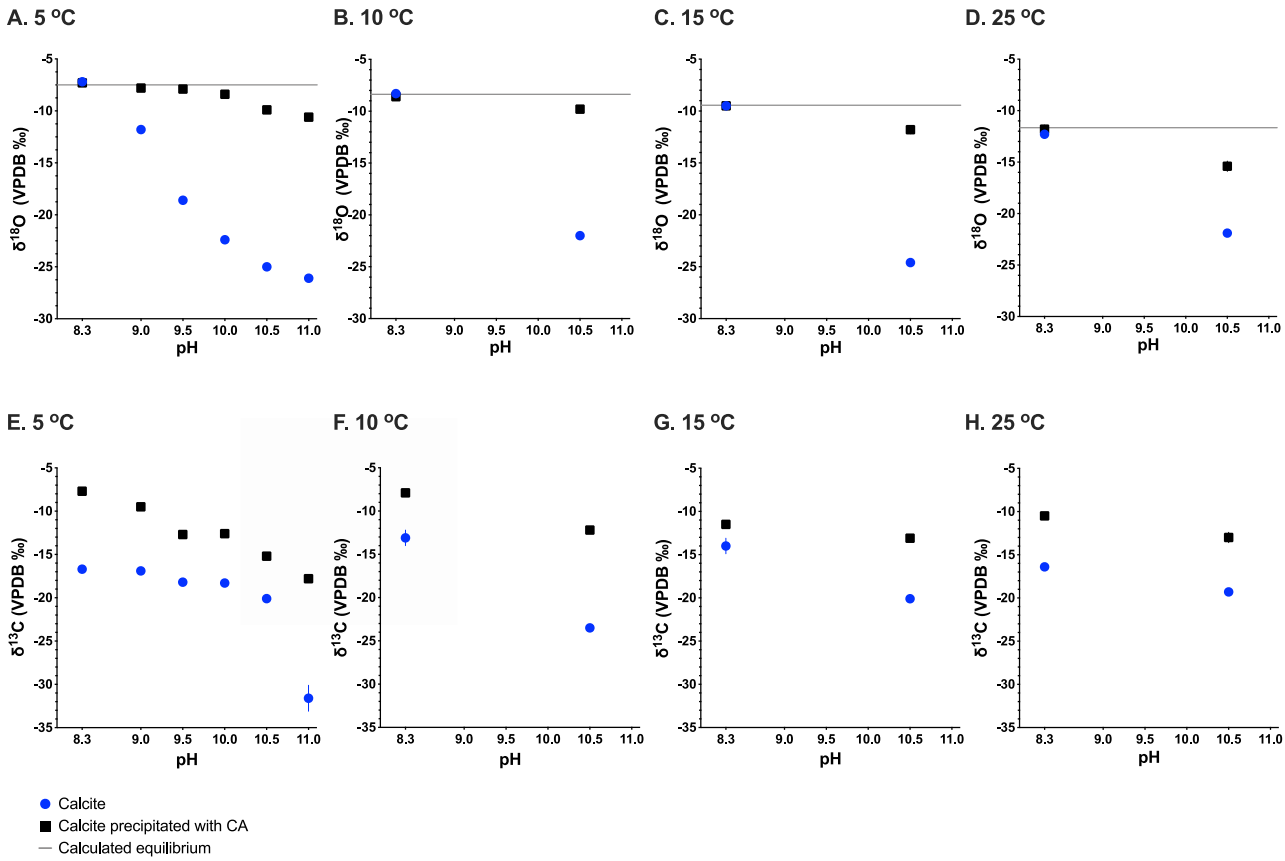

Figure 2. The $\delta^{18}O$ and $\delta^{13}C$ values versus precipitation pH for calcite precipitated with CA (black squares) and without CA (blue circles). The $\delta^{18}O$ versus precipitation pH for (a) 5°C, (b) 10°C, (c) 15°C, and (d) 25°C, and $\delta^{13}C$ versus precipitation pH for (e) 5°C, (f) 10°C, (g) 15°C, and (h) 25°C show depleted values with increased pH. The oxygen isotope equilibrium values (gray line) were calculated from Kim and O'Neil (1997). Error bars indicate 1 SD and in some cases are smaller than the symbol.

precipitated with CA, and these samples also had negative Δ_{48} values (i.e., $^{12}C^{18}O^{18}O$ occurring less frequently than predicted by a stochastic distribution) (Figure 3, Table 3). The enrichment of Δ_{47} and depletion of Δ_{48} increased with increasing pH. The largest Δ_{47} enrichment was 0.203‰ at 5°C and pH 10.5. The largest Δ_{48} depletion was −0.693‰ at 5°C and pH 11.0. Despite the larger depletions in Δ_{48} than enrichments in Δ_{47}, CA appears to be more effective at returning Δ_{48} values to near-equilibrium values than for Δ_{47}.

Kinetic slopes for $\Delta_{47}/\delta^{18}O$, $\Delta_{48}/\delta^{18}O$, and Δ_{47}/Δ_{48} were determined (Table 4). Kinetic slopes for $\Delta_{47}/\delta^{18}O$ (Figures 4a–4d) at 5°C, 10°C, 15°C, and 25°C were −0.011 ± 0.001, −0.013 ± 0.001, −0.012 ± 0.002, and −0.020 ± 0.001, respectively. Kinetic slopes for $\Delta_{48}/\delta^{18}O$ (Figures 4e–4h) at 5°C, 10°C, 15°C, and 25°C were 0.036 ± 0.002, 0.045 ± 0.0001, 0.036 ± 0.0001, and 0.055 ± 0.002, respectively. Kinetic slopes for Δ_{47}/Δ_{48} (Figure 5) at 5°C, 10°C, 15°C, and 25°C were −0.301 ± 0.014, −0.292 ± 0.009, −0.318 ± 0.006, and −0.354 ± 0.004, respectively.

Equilibrium regressions were made for Δ_{47} and Δ_{48} versus precipitation temperature (Figures 6a and 6b), Δ_{47} and Δ_{48} versus $\delta^{18}O$ (Figures 6c and 6d), and Δ_{47}-Δ_{48} (Figure 6e), for calcite precipitated at 5°C, 10°C, 15°C, and 25°C with CA at pH 8.3, which are expected to achieve isotopic equilibrium. Devils Hole core DH-2 data previously analyzed in Lucarelli, Carroll, et al. (2023) were included in the equilibrium regressions for Δ_{47}-Δ_{48}, Δ_{47}-T, and Δ_{48}-T. Devils Hole has been shown to be near isotopic equilibrium (Coplen, 2007; Winograd et al., 1992) and has a known precipitation temperature of 33.7 ± 0.2°C (Plummer et al., 2000). The experimental Δ_i versus temperature relationships were determined to be

$$\Delta_{47\ \text{I-CDES}} = (0.038\ \pm 0.003) \times 10^6\ T^{-2} + (0.161\ \pm 0.032);\ r^2 = 0.99 \quad (7)$$

$$\Delta_{48\ \text{CDES 90}} = (0.015\ \pm 0.002) \times 10^6\ T^{-2} + (0.076\ \pm 0.025);\ r^2 = 0.94 \quad (8)$$

Table 3
Clumped and Stable Isotope Data for All Samples Measured in This Study

Temperature (°C)	pH	CA (yes or no)	Δ_{47} I-CDES (‰)	SD	SE	N	Δ_{48} CDES 90 (‰)	SD	SE	N	Δ_{63} (‰)	Δ_{64} (‰)	$\delta^{18}O$ VPDB (‰)	SD	1000 ($\alpha_{calcite-H_2O}$)	$\delta^{13}C$ VPDB (‰)	SD
5	8.3	Y	0.651	0.017	0.004	15	0.273	0.060	0.019	10	0.454	0.142	−7.3	0.1	32.8	−7.7	0.0
5	8.3	N	0.655	0.014	0.006	5	0.279	0.042	0.021	4	0.458	0.148	−7.2	0.1	32.7	−16.7	0.1
5	9.0	Y	0.652	0.025	0.007	13	0.261	0.053	0.024	5	0.455	0.130	−7.8	0.1	32.0	−9.5	0.1
5	9.0	N	0.648	0.029	0.009	10	0.230	0.017	0.005	10	0.451	0.099	−11.8	0.1	28.2	−16.9	0.1
5	9.5	Y	0.663	0.019	0.005	12	0.256	0.073	0.026	8	0.466	0.125	−7.9	0.1	32.0	−12.7	0.1
5	9.5	N	0.749	0.022	0.009	6	−0.181	0.052	0.018	8	0.551	−0.309	−18.6	0.1	21.1	−18.2	0.1
5	10.0	Y	0.652	0.011	0.004	7	0.266	0.033	0.015	5	0.455	0.135	−8.4	0.1	31.2	−12.6	0.0
5	10.0	N	0.814	0.024	0.008	10	−0.257	0.014	0.007	4	0.614	−0.384	−22.4	0.2	18.6	−18.3	0.0
5	10.5	Y	0.712	0.017	0.006	7	0.242	0.046	0.020	5	0.514	0.111	−9.9	0.2	30.3	−15.2	0.1
5	10.5	N	0.854	0.016	0.005	10	−0.320	0.053	0.020	7	0.654	−0.447	−25.0	0.1	14.8	−20.1	0.0
5	11.0	Y	0.686	0.025	0.008	9	0.265	0.024	0.011	5	0.489	0.134	−10.6	0.1	29.6	−17.8	0.0
5	11.0	N	0.845	0.014	0.007	4	−0.420	0.158	0.071	5	0.645	−0.546	−26.1	0.1	n/a	−31.6	1.5
10	8.3	Y	0.636	0.019	0.007	8	0.260	0.064	0.021	9	0.440	0.129	−8.6	0.2	31.4	−7.9	0.2
10	8.3	N	0.634	0.014	0.005	9	0.274	0.027	0.012	5	0.438	0.143	−8.3	0.4	31.4	−13.1	0.9
10	10.5	Y	0.707	0.028	0.009	9	0.249	0.092	0.035	7	0.509	0.118	−9.8	0.0	29.7	−12.2	0.3
10	10.5	N	0.804	0.028	0.008	11	−0.326	0.063	0.028	5	0.605	−0.452	−22.0	0.2	17.3	−23.5	0.1
15	8.3	Y	0.626	0.027	0.008	12	0.259	0.029	0.011	7	0.430	0.128	−9.5	0.4	30.3	−11.5	0.1
15	8.3	N	0.629	0.018	0.006	10	0.261	0.055	0.024	5	0.433	0.130	−9.5	0.3	29.9	−14.0	0.9
15	10.5	Y	0.694	0.023	0.007	10	0.172	0.062	0.025	6	0.497	0.042	−11.8	0.4	28.1	−13.1	0.3
15	10.5	N	0.801	0.024	0.007	13	−0.285	0.096	0.039	6	0.602	−0.412	−24.6	0.3	14.9	−20.1	0.1
25	8.3	Y	0.594	0.033	0.008	17	0.250	0.026	0.010	7	0.399	0.119	−11.8	0.4	28.1	−10.5	0.2
25	8.3	N	0.591	0.034	0.010	12	0.252	0.024	0.007	12	0.396	0.121	−12.3	0.4	27.5	−16.4	0.2
25	10.5	Y	0.746	0.012	0.005	7	0.169	0.108	0.054	4	0.548	0.039	−15.4	0.5	24.8	−13.0	0.6
25	10.5	N	0.788	0.029	0.009	11	−0.302	0.079	0.035	5	0.589	−0.429	−21.9	0.2	18.1	−19.3	0.3

Note. Calcite mineral Δ_{63} and Δ_{64} was calculated using equations from Lucarelli, Carroll, et al. (2023).

where T is the precipitation temperature in Kelvin. The Δ_{47}-Δ_{48} relationship is represented by Equation 9.

$$\Delta_{47\ \text{I-CDES}} = (2.43 \pm 0.289)\ \Delta_{48\ \text{CDES 90}} - (0.006 \pm 0.074);\ r^2 = 0.96 \quad (9)$$

The equilibrium relationships for Δ_{47} and Δ_{48} versus $\delta^{18}O$ are represented by Equations 10 and 11.

$$\Delta_{47\ \text{I-CDES}} = (0.013 \pm 0.001)\ \delta^{18}O_{\text{VPDB}} + (0.743 \pm 0.006);\ r^2 = 0.99 \quad (10)$$

$$\Delta_{48\ \text{CDES 90}} = (0.005 \pm 0.001)\ \delta^{18}O_{\text{VPDB}} + (0.304 \pm 0.010);\ r^2 = 0.97 \quad (11)$$

3.1.3. Measured and Modeled Δ_{47}, Δ_{48}, $\alpha_{\text{calcite-water}}$, and Growth Rate Effects

Figure 7 compares our calcite isotopic values for samples grown without CA (blue symbols) to those predicted for HCO_3^- and CO_3^{2-} endmembers as a function of time (purple and green curves) using the IsoDIC model (Guo, 2020). Specifically, we used the model to quantify the temporal evolution of Δ_{63} and Δ_{64} values in HCO_3^- and CO_3^{2-} endmembers during CO_2 absorption in an aqueous solution at pH 10.5 at 5 and 25°C. The model trajectories, which had a total evolution time of 12 hr, agree with titration data indicating that in experiments with pH ≥ 9.5 at 5 and 25°C, calcite precipitation began during the first day. At both temperatures, the calcite precipitated at pH 10.5 exceeded the model predictions for maximum enrichment of Δ_{63}, and conversely, it did

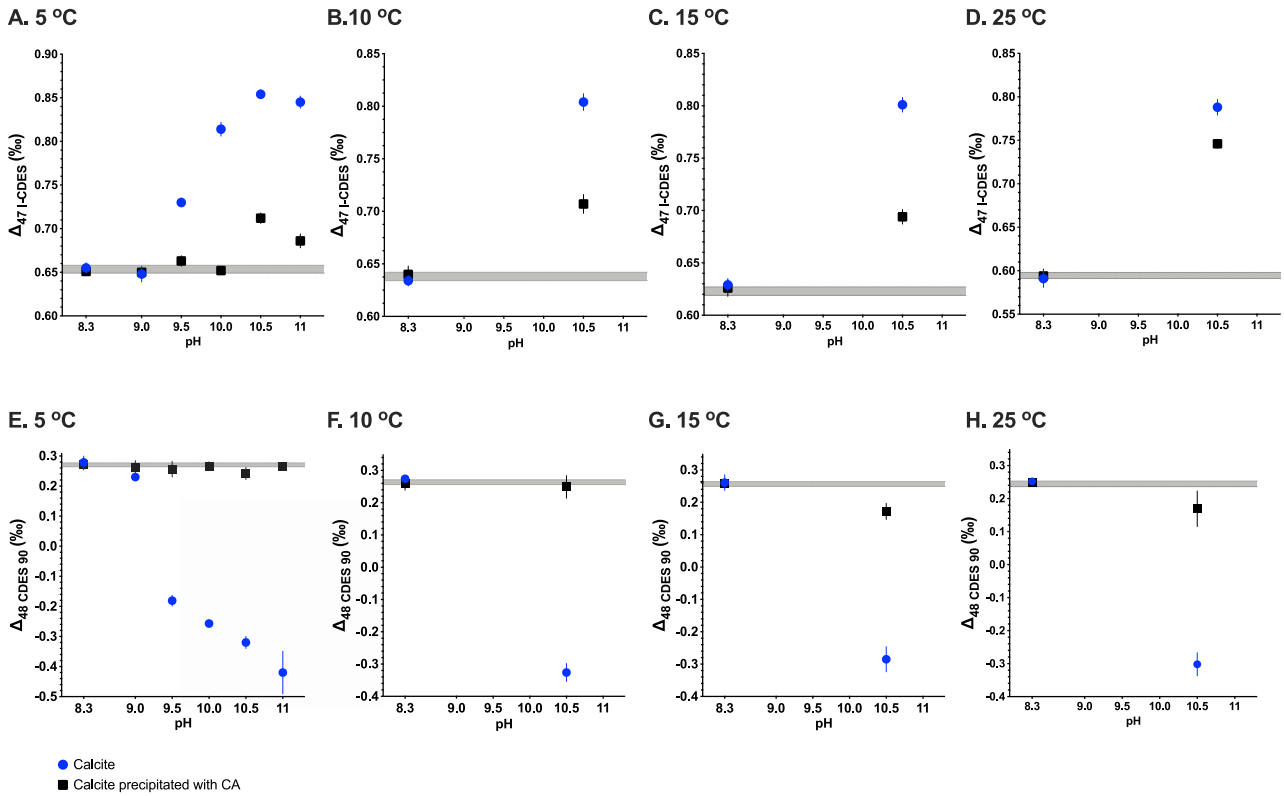

Figure 3. Clumped isotope values versus precipitation pH at variable temperature for calcite precipitated with CA (black squares) and without CA (blue circles). The Δ_{47} versus pH at (a) 5°C, (b) 10°C, (c) 15°C, and (d) 25°C, and Δ_{48} versus pH at (e) 5°C, (f) 10°C, (g) 15°C, and (h) 25°C show increases in Δ_{47} and decreases in Δ_{48} in samples precipitated at pH ≥ 9.5. The gray bar is the range of expected equilibrium values derived from Swart et al. (2021), Fiebig et al. (2021), Lucarelli, Carroll, et al. (2023), and this study. Error bars indicate 1 SE.

not achieve the maximum amount of depletion for Δ_{64} predicted by the model, which could indicate the influence of another factor, such as the growth rate.

For calcite precipitated at high pH, the addition of with CA reduced kinetic bias, resulting in distinct kinetic trajectories (black lines in Figure 7). The Δ_{47}/Δ_{48} slopes for these samples were steeper than for samples precipitated at high pH without CA, with Δ_{47}-Δ_{48} slopes of $m = -0.371 \pm 0.107$ at 5°C and $m = -0.443$ at 25°C. Increased disequilibrium was observed in Δ_{47} relative to Δ_{48} in samples at pH ≥ 9.5 with CA, indicating that CA may have greater efficiency for equilibrating *m/z* 64 isotopologues than *m/z* 63 isotopologues. Since *m/z* 63 isotopologues contain both ^{13}C and ^{18}O, it may take longer to equilibrate than *m/z* 64 isotopologues, which

Table 4
Equilibrium and Kinetic Slopes for Clumped and Bulk Isotopes

Temperature (°C)	Equilibrium or kinetic	Slope: $\Delta_{47\ \text{I-CDES}}/\delta^{18}O_{\text{VPDB}}$	SE	Slope: $\Delta_{48\ \text{CDES 90}}/\delta^{18}O_{\text{VPDB}}$	SE	Slope: $\Delta_{47\ \text{I-CDES}}/\Delta_{48\ \text{CDES 90}}$	SE	Slope: Δ_{63}/Δ_{64}
5–33.7	Equilibrium	0.013	0.001	0.005	0.001	2.43	0.289	2.68
5	Kinetic	−0.011	0.001	0.036	0.002	−0.301	0.014	−0.294
10	Kinetic	−0.013	0.001	0.045	0.0001	−0.292	0.009	−0.322
15	Kinetic	−0.012	0.002	0.036	0.0001	−0.318	0.006	−0.334
25	Kinetic	−0.020	0.001	0.055	0.002	−0.354	0.004	−0.345

Note. Equilibrium slopes were determined from calcite samples precipitated at pH 8.3 with CA at 5°C, 10°C, 15°C, and 25°C, and Devils Hole calcite. Kinetic slopes at 5°C were determined with a regression through samples precipitated at pH 8.3 with and without CA, and pH 9.5, 10.0, 10.5, and 11.0 without CA. Kinetic slopes at 10°C, 15°C, and 25°C were determined by regressions through samples precipitated at pH 8.3 with and without CA, and at pH 10.5 without CA. Calcite mineral Δ_{63} and Δ_{64} were calculated using equations from Lucarelli, Carroll, et al. (2023).

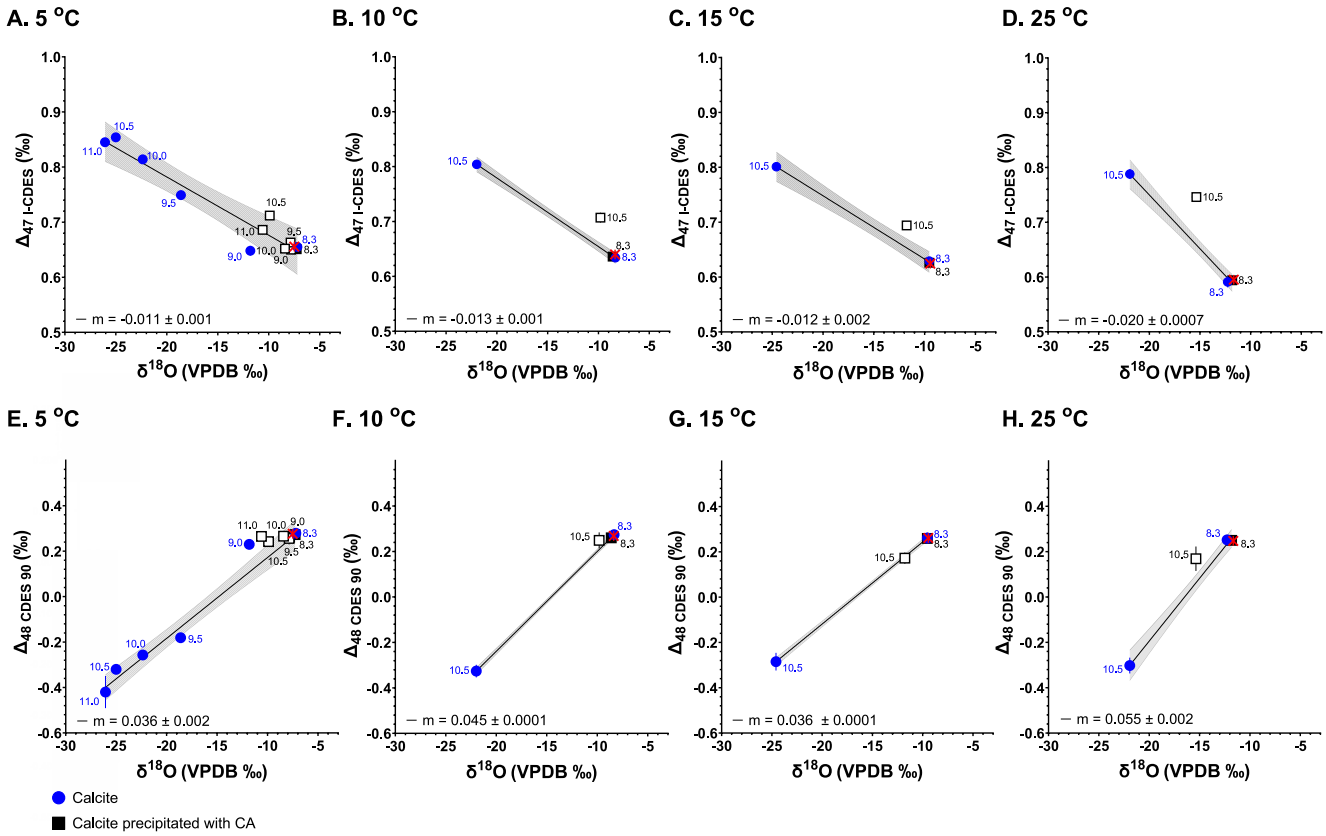

Figure 4. Clumped and oxygen isotope values for calcite precipitated with CA (black squares) and without CA (blue circles) at variable temperature and pH. The Δ_{47} versus $\delta^{18}O$ values at (a) 5°C ($r^2 = 0.96$), (b) 10°C ($r^2 = 0.99$), (c) 15°C ($r^2 = 0.99$), and (d) 25°C ($r^2 = 0.99$), and Δ_{48} versus $\delta^{18}O$ values at (e) 5°C ($r^2 = 0.99$), (f) 10°C ($r^2 = 0.99$), (g) 15°C ($r^2 = 0.99$), and (h) 25°C ($r^2 = 0.99$). Numbers next to each data point indicate the precipitation pH. Calcite precipitated at pH ≥ 9.5 without CA (blue circles) is depleted in $\delta^{18}O$ and Δ_{48} and enriched in Δ_{47} relative to samples precipitated at lower pH, or higher pH with CA (black squares). They are also depleted relative to expected equilibrium values (red X), where the equilibrium values were calculated from Kim and O'Neil (1997) and Fiebig et al. (2021). Regressions (black line) with 95% confidence interval (gray shading) include quasi-equilibrium samples precipitated at pH 8.3 and samples precipitated at elevated pHs without CA, with negative slopes for $\Delta_{47}/\delta^{18}O$, and positive slopes for $\Delta_{48}/\delta^{18}O$. Data for calcite precipitated at pH ≥ 9.0 with CA (open black squares) show less kinetic bias and were not included in the regressions. Error bars indicate 1 SE for clumped isotope values and 1 SD for oxygen isotope values, and in some cases are smaller than the symbol.

contain 2 ^{18}O atoms and no ^{13}C, due to CA catalyzing O isotope exchange. It has been shown experimentally that CA discriminates against CO_2 and HCO_3^- that contain ^{13}C due to slower rates of diffusion to the enzyme (Paneth & O'Leary, 1985).

We compare our experimental results to box model calculations that factor into account modulation of isotopic fractionation by the growth rate (Figure 8). We used the model to predict $1000\ln(\alpha_{\text{calcite-water}})$, $\delta^{13}C$, Δ_{47}, and Δ_{48} with and without CA. We also compared our results to experimental data from Tang et al. (2014) (Figure 8). Tang et al. (2014) performed calcite precipitation experiments at pH 8.3, 8.5, 9.0, 9.5, 10.0, and 10.5 at 5°C, and pH 8.3 at 25°C, with precipitation rates (R) ranging from −5.99 to −7.38. Our precipitation rates are given as the log of R (mol m^{-2} s^{-1}) for direct comparability to previous modeling and measurements (Table 1). The precipitation rates measured here range from −7.02 to −7.48, which are typical growth rates for calcite precipitation experiments or for corals, which range from ∼−4.8 to ∼−7.6 (Dietzel et al., 2009; Ghosh et al., 2006; Saenger et al., 2012).

The model results for $1000\ln(\alpha_{\text{calcite-water}})$ at 5 and 25°C (Figure 8) have good agreement with the observed experimental fractionations at high pH for samples without CA. The samples at 5°C with CA have $1000\ln(\alpha_{\text{calcite-water}})$ values that are closer to the kinetic limit (red curve) than predicted by the model calculations, which consider the addition of 0.25 μM CA. The model-predicted values for Δ_{47} and Δ_{48} had better agreement with experimental values at low pH, and high pH at 25°C, with the sample at 5°C and pH 11.0 offset from model predictions by ∼0.19‰. The model does not explain the measured changes in $\delta^{13}C$ values.

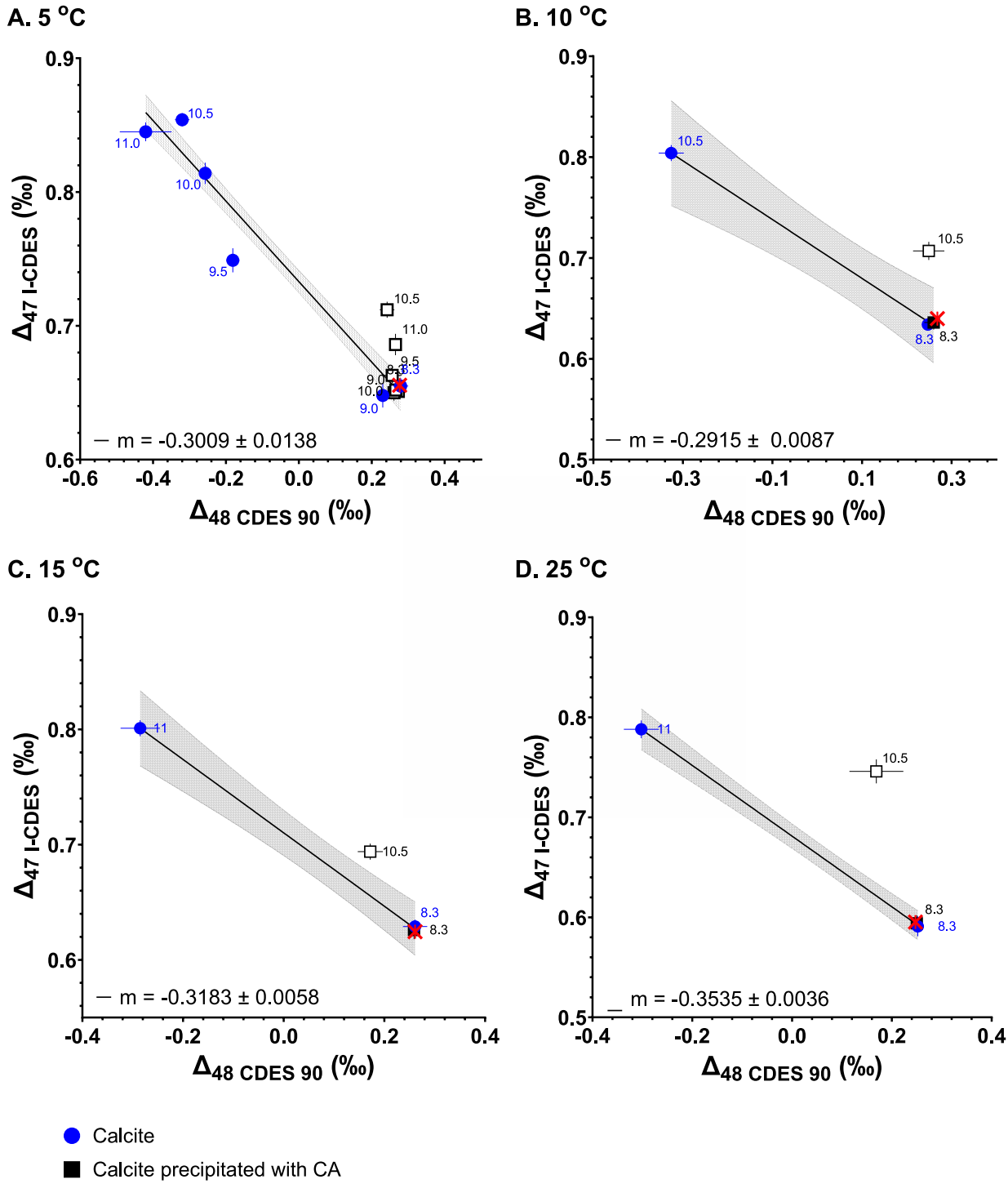

Figure 5. The Δ_{47} and Δ_{48} values for calcite precipitated at variable pH with CA (black squares) and without CA (blue circles) at (a) 5°C ($r^2 = 0.95$), (b) 10°C ($r^2 = 0.99$), (c) 15°C ($r^2 = 0.99$), and (d) 25°C ($r^2 = 0.99$). Numbers next to each data point indicate the precipitation pH. Regressions (black line) with 95% confidence interval (gray shading) are between quasi-equilibrium samples precipitated at pH 8.3 and samples precipitated at elevated pHs without CA, with enrichments in Δ_{47} and depletions Δ_{48} relative to equilibrium (red X) observed for all experiments. Data for calcite precipitated at pH ≥ 9.0 with CA (open black squares) had less kinetic bias and not included in the regressions. Equilibrium values were calculated from Fiebig et al. (2021). Error bars indicate 1 SE.

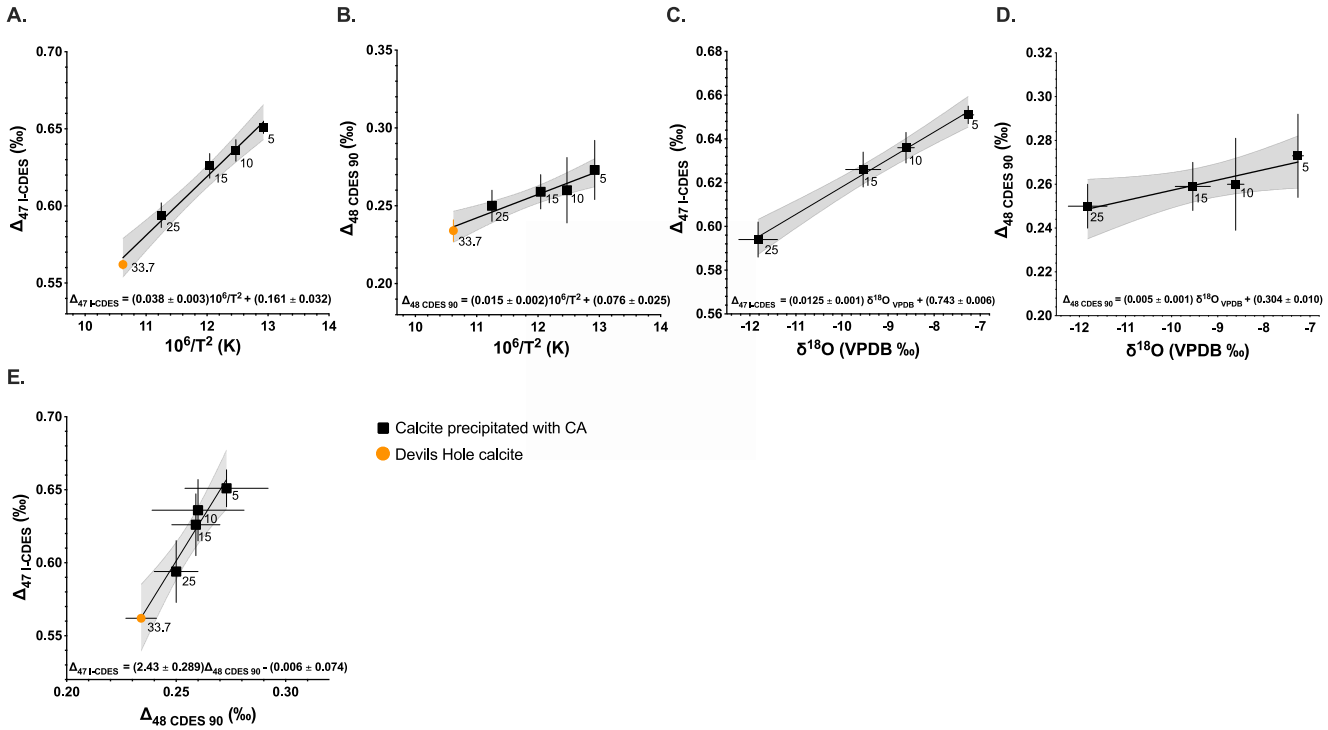

Figure 6. Quasi-equilibrium regressions for clumped isotope data versus precipitation temperature for (a) Δ_{47}-10^6T^{-2} ($r^2 = 0.99$) and (b) Δ_{48}-10^6T^{-2} ($r^2 = 0.94$), with temperature in Kelvin. Quasi-equilibrium regressions for (c) Δ_{47}-$\delta^{18}O$ ($r^2 = 0.99$) and (d) Δ_{48}-$\delta^{18}O$ ($r^2 = 0.97$). Quasi-equilibrium regression for (e) Δ_{47}-Δ_{48} ($r^2 = 0.96$). All regressions (black lines) are shown with the 95% confidence interval (gray shading). Data on all panels is for samples precipitated at pH 8.3 with CA (black squares) and for Devils Hole calcite (DH-2) (orange circles), which is thought to have formed near isotopic equilibrium at a temperature of 33.7 ± 0.2°C (Bajnai et al., 2021; Coplen, 2007; Daëron et al., 2019; Lucarelli, Carroll, et al., 2023; Tripati et al., 2015; Winograd et al., 1992, 1988). The precipitation temperature is indicated next to each symbol in Celsius. Error bars indicate 1 SE for clumped isotopes and 1 SD for oxygen isotopes.

4. Discussion

4.1. Comparison of Kinetic Effects Observed in Isotopic Data With Theory

4.1.1. $\delta^{18}O$ and $\delta^{13}C$

There are multiple factors that may contribute to the observed clumped and bulk KIEs in this study, including CO_2 hydration and hydroxylation, pH dependent DIC speciation, growth rate effects, diffusive isotope effects, and precipitation occurring before temperature and pH dependent equilibrium is achieved in the DIC pool. Modeling predicts that hydration should discriminate against ^{18}O by 14–15‰ and ^{13}C by 19–23‰ at 25°C, while hydroxylation would discriminate against ^{18}O by 27–30‰ and ^{13}C by 26–31‰ at 25°C (Boettger & Kubicki, 2021). At a pH > ~8.4 hydroxylation starts to dominate, and at a pH of 10, hydroxylation represents 95% of reactions (McConnaughey, 1989). Additionally, at equilibrium, $\delta^{18}O$ decreases in DIC species in the following order: $CO_2 > H_2CO_3 > HCO_3^- > CO_3^{2-}$ (Beck et al., 2005; Usdowski et al., 1991), and at pH > 10, CO_3^{2-} dominates the DIC composition (Hill et al., 2014; Tripati et al., 2015). This is consistent with what we experimentally observed, with increasing depletion in oxygen isotopes starting in samples precipitated at pH ≥ 9 without CA (Table 3, Figure 2).

The trend observed in $\delta^{13}C$ also indicates subtle depletion starting at pH ≥ 9.5 for samples precipitated without CA (Figure 2). For calcite precipitated with CA, there was depletion starting at pH ≥ 9. When calcite precipitated with and without CA at the same pH and temperature were directly compared, there was an offset observed in $\delta^{13}C$, including for samples precipitated at pH 8.3 (Table 3, Figure 2). This offset may be due to diffusion and the effects of CA on the CO_2 gradient between the inner and outer solutions. The enzyme CA increases the rate of inter-conversion between CO_2 and HCO_3^-, and thus, the [CO_2] in the outer solution could be higher in experiments with CA. If so, this would decrease the CO_2 gradient between the inner and outer chambers and lead to less

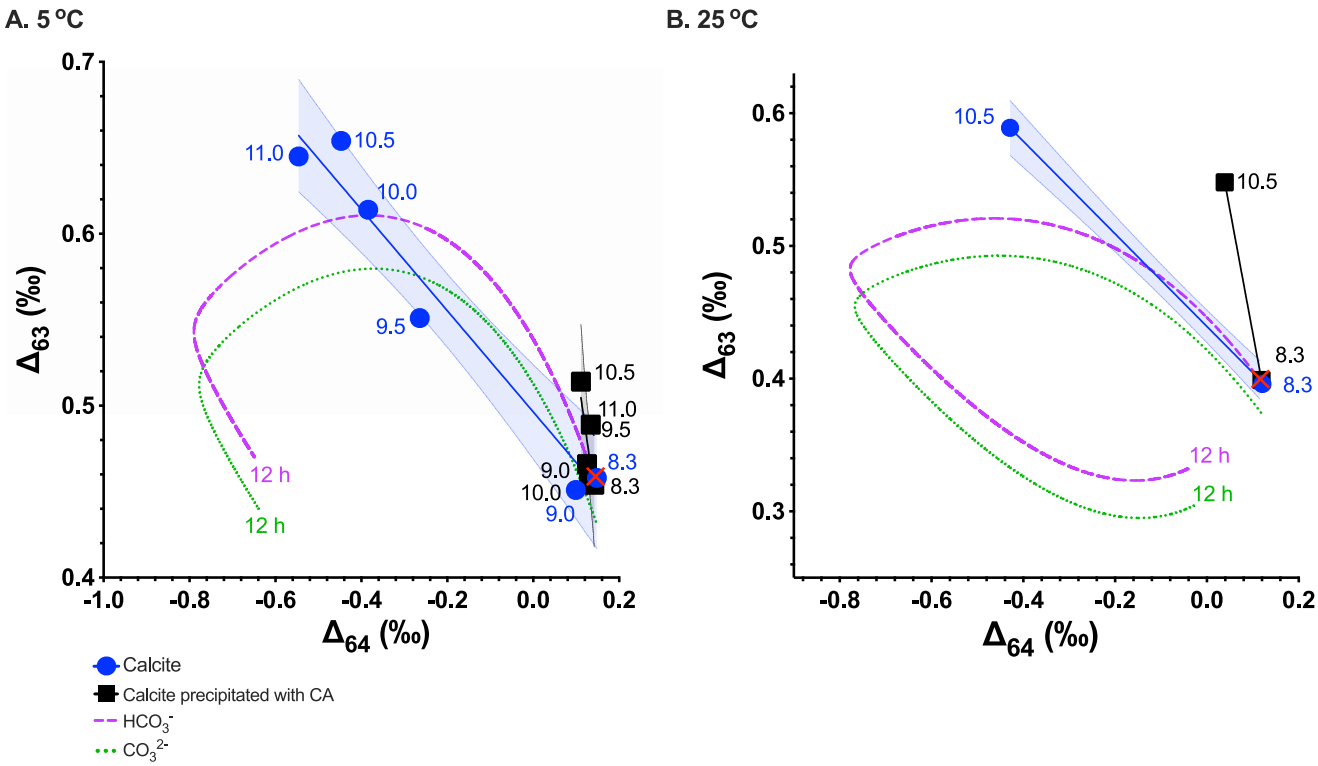

Figure 7. Experimental results compared to IsoDIC model predictions for the evolution of HCO_3^- (purple dashed line) and CO_3^{2-} (green dotted line) isotopic compositions for an evolution time of 12 hr at (a) 5°C and pH 10.5 and (b) 25°C and pH 10.5. Experimental data are for calcite precipitated without CA (blue circles) and calcite precipitated with CA (black squares) at varying pH. Numbers by data points indicate pH of the precipitation solution. Regressions are shown for calcite (blue line) and calcite with CA (black line) with the 95% confidence interval (shaded area). The IsoDIC software we used for model calculations is from Guo (2020). The predicted equilibrium values (red X) were calculated by converting equilibrium Δ_{47} and Δ_{48} values from Fiebig et al. (2021) into Δ_{63} and Δ_{64} values, respectively, using equations from Lucarelli, Carroll, et al. (2023).

diffusive isotopic fractionation. For samples precipitated without CA in the outer solutions, the CO_2 diffusing into the outer chamber would be isotopically lighter, which is consistent with observations.

This same effect is not evident in $\delta^{18}O$, with catalyzed and uncatalyzed experiments at pH 8.3 and the same temperature having statistically indistinguishable $\delta^{18}O$ values (Figure 2). However, CA catalyzes the pathway for O exchange among DIC species to a nearly instantaneous reaction but does not catalyze the exchange of C among DIC species.

4.1.2. Dual Clumped Isotopes (Δ_{47}-Δ_{48} and Δ_{63}-Δ_{64}) and Clumped Isotopes With $\delta^{18}O$

Calcite precipitated at pH ≥ 9.5 exhibits enriched Δ_{47} and depleted $\delta^{18}O$ and Δ_{48} values relative to calcite precipitated at lower pH or elevated pH with CA (Figures 3 and 4), consistent with CO_2 hydrolysis (Guo, 2020; Tripati et al., 2015). These samples also exhibit negative Δ_{48} values, termed "anti-clumped" (Douglas et al., 2017; Fiebig et al., 2021), potentially from a depletion in $^{12}C^{18}O^{18}O$ produced by the relative rate kinetics for different CO_2 isotopologues during hydration and hydroxylation. A similar pattern was observed in calcite samples taken from naturally alkaline springs (pH = 11.5) associated with the Cedars peridotite formation reported in Parvez et al. (2023). The Cedars samples had a maximum observed enrichment for Δ_{47} of 0.163‰ and a maximum depletion for Δ_{48} of −0.761‰. This is consistent with the maximum enrichment for Δ_{47} of 0.203‰ and a maximum depletion for Δ_{48} of −0.693‰ observed here. Our data yield kinetic Δ_{47}/Δ_{48} slopes that range between −0.292 and −0.354 (Figure 5). These slopes are in good agreement with the Δ_{47}/Δ_{48} slope of −0.310 observed for the Cedars samples (Figure 9). Additionally, the slopes observed here and for the Cedars samples fall between theoretical slopes (Guo, 2020) for CO_2 absorption (pH = 9) and high pH travertines (pH = 11.5), of −0.58 and −0.12, respectively (Figure 9).

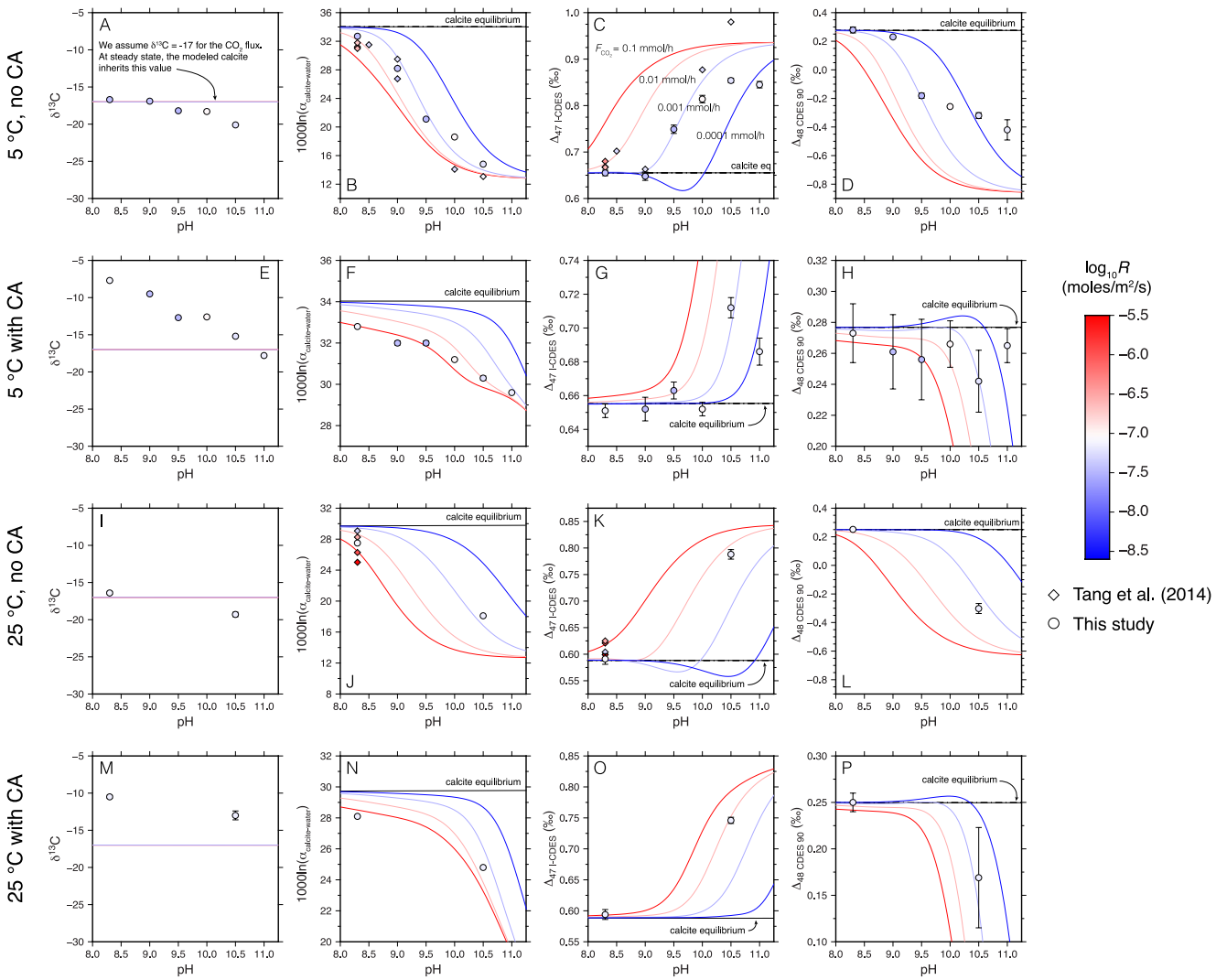

Figure 8. Experimental results from this work (circles) compared to data from Tang et al. (2014) (diamonds) and box model predictions (curves). Curves show $\delta^{13}C$ (panels a, e, i, m), $1000\ln(\alpha_{calcite\text{-}water})$ (panels b, f, j, n), Δ_{47} (panels c, g, k, o), and Δ_{48} (panels d, h, l, p) of calcite predicted by the box model for different values of F_{CO2} at 5°C (top two rows) and 25°C (bottom two rows). Higher F_{CO2} translates to faster growth rate. Colors indicate growth rate with color scale shown, where blue is slow growth and red is fast growth. Measured and modeled data indicate that calcite precipitated at pH ≥ 9.5 has KIEs that enrich Δ_{47} (panels c, d) and deplete Δ_{48} values (panels k, l) relative to equilibrium (black line). Measured and modeled data also indicate that calcite precipitated at pH ≥ 9 has KIEs that deplete oxygen isotope values relative to equilibrium (black line), plotted as $1000\ln(\alpha_{calcite\text{-}water})$ (panels b, j). The addition of CA into the precipitation fluid largely removes the KIEs observed in both oxygen and clumped isotopes (f–h, n–p). For $\delta^{13}C$ (1st column), the model does not explain the measured pH-dependence. In the model, we treat the isotopic composition of the CO_2 flux as a constant and find that the model predicts calcite to inherit the input value. The data therefore suggest that the $\delta^{13}C$ of incoming CO_2 (g) varies between experiments potentially from diffusion through the plastic membrane.

We were able to simulate anti-clumped Δ_{64} values that are consistent with our experimental observations for Δ_{48}. Our measured kinetic slopes at 25°C for $\Delta_{47}/\delta^{18}O$ of −0.020 ± 0.001, and $\Delta_{48}/\delta^{18}O$ of 0.055 ± 0.002 (Figure 4, Table 4) are in good agreement with model predicted slopes for hydration/hydroxylation during CO_2 absorption of −0.024 for $\Delta_{47}/\delta^{18}O$ and 0.041 for $\Delta_{48}/\delta^{18}O$ (Guo, 2020). This agreement indicates that hydration and hydroxylation KIEs occurring during CO_2 absorption are likely the most significant KIEs observed in our samples precipitated at higher pHs.

In our 5°C sample at pH 9, there was a depletion in $\delta^{18}O$ of 4‰ relative to the calcite precipitated with CA under the same conditions, and no statistically significant change in Δ_{47} (Table 3). This may indicate that carbonates precipitated at pH ≤ 9 are more likely to exhibit a decoupling of disequilibrium in $\delta^{18}O$ and Δ_{47}, but calcite precipitated at pH ≥ 9.5 exhibit disequilibrium in both $\delta^{18}O$ and Δ_{47} values. It should also be noted that our 5°C sample at pH 9 had a Δ_{48} depletion of 0.042‰ relative to expected equilibrium, possibly indicating a greater

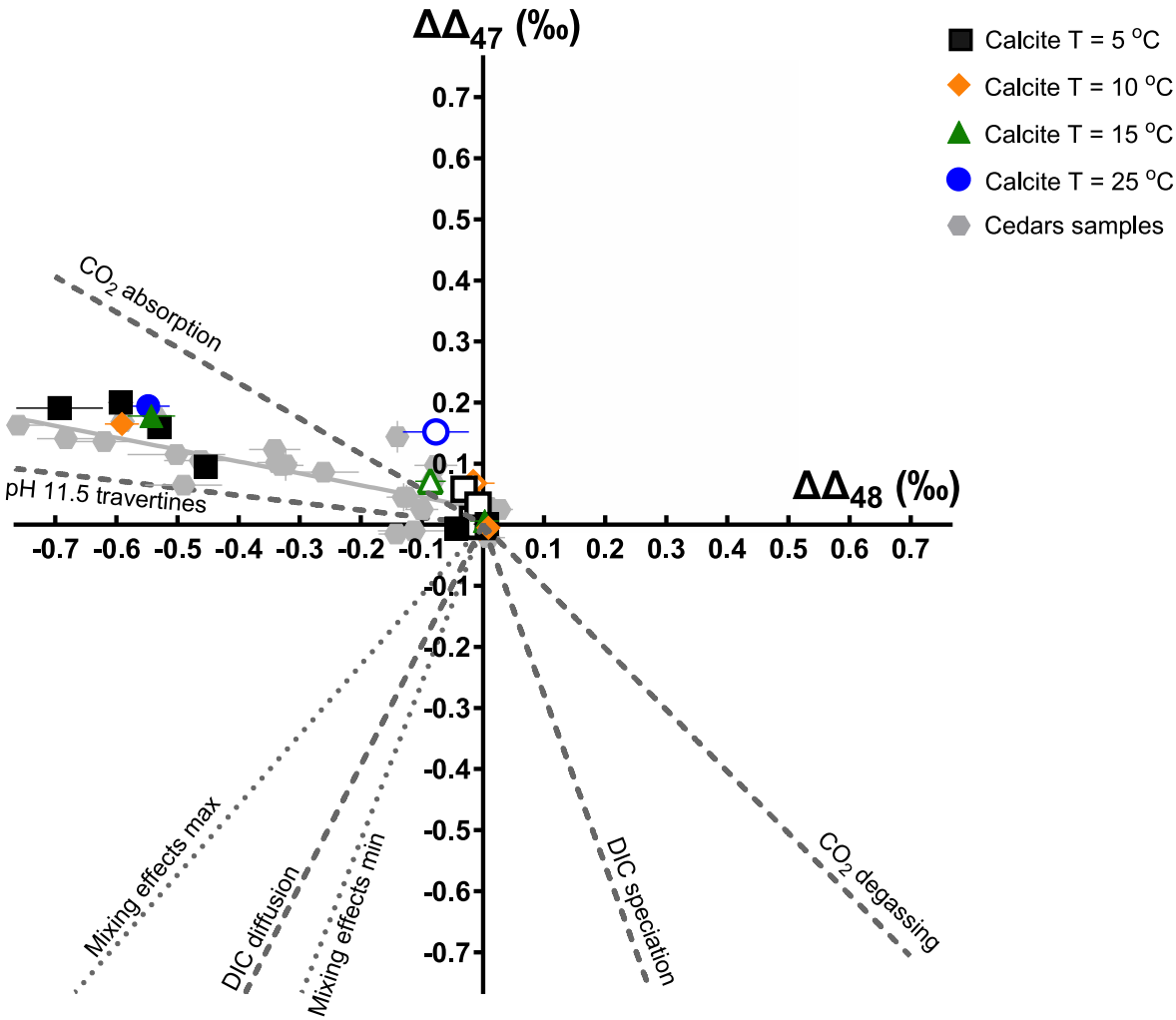

Figure 9. The $\Delta\Delta_{47}$ versus $\Delta\Delta_{48}$ values, calculated as $\Delta_{i\ measured} - \Delta_{i\ equilibrium}$, from this work compared to samples from natural high pH springs and theoretical predictions. Colored symbols are for calcite from this study synthesized at different temperatures and pHs. Open symbols are for samples precipitated with CA. Carbonate minerals from highly alkaline springs at the Cedars, California from Parvez et al. (2023) are shown (gray hexagons) with their kinetic slope (solid gray line). The slope from the Cedars samples of −0.310 is in good agreement with samples from this study, which have slopes of −0.301, −0.292, −0.318, and −0.354 for 5°C, 10°C, 15°C, and 25°C, respectively (Figure 5). Theoretical slopes are shown for HCO_3^- endmembers produced through varying kinetic processes (gray dashed lines; Guo, 2020), and mixing model predictions for calcite (gray dotted lines; Lucarelli, Purgstaller, et al., 2023). Slopes for DIC speciation = −2.790; DIC diffusion = 1.970; CO_2 degassing at pH 8 = −1.010; CO_2 absorption at pH 9 = −0.580; travertine precipitation at pH 11.5 = −0.120; mixing = 1.147 to 2.584. The $\Delta_{i\ equilibrium}$ values were from samples precipitated at pH 8.3 with CA. Error bars indicate 1 SE.

sensitivity to pH and disequilibrium oxygen isotope values than for Δ_{47}, due to the presence of two ^{18}O substitutions in *m/z* 64 isotopologues. This may represent the same type of decoupling between oxygen isotopes and Δ_{47} that were observed in deep-sea corals (Thiagarajan et al., 2011).

4.1.3. The Effect of Precipitation Rate on Bulk and Clumped Isotopes

KIEs resulting in disequilibrium clumped isotope compositions of DIC have the potential to be recorded in carbonate minerals, modulated by growth rate (Tripati et al., 2015; Watkins & Hunt, 2015). It has been suggested that at rapid growth rates, a kinetic limit may be reached, while at slow growth, an equilibrium limit may be attained (e.g., DePaolo, 2011; Tripati et al., 2015; Watkins and Hunt, 2015). For example, Watkins and Hunt (2015) used an ion-by-ion growth model to predict calcite grown at typical experimental growth rates ($\log_{10} R = -5$ to -7 mol/m^2/s) from a solution with a fully equilibrated DIC pool at pH 8–9 and 25°C should be at or near the kinetic limit resulting in Δ_{63} that is ~0.01‰ higher than equilibrium. For samples precipitated at pH > 10, calcite would be ~0.01 to ~0.02‰ lower than expected equilibrium Δ_{63} values. The kinetic limit should be substantially different if

Table 5
Comparison of Measured Equilibrium Δ_{47} and Δ_{48} Values From This Study and Previously Published Results

T (°C)	$\Delta_{47\ \text{I-CDES}}$ (this study) (‰)	SE	$\Delta_{47\ \text{CDES 90}}$ (Swart et al., 2021) (‰)	SE	$\Delta_{47\ \text{CDES 90}}$ (Fiebig et al., 2021) (‰)	$\Delta_{48\ \text{CDES 90}}$ (this study) (‰)	SE	$\Delta_{48\ \text{CDES 90}}$ (Swart et al., 2021) (‰)	SE	$\Delta_{48\ \text{CDES 90}}$ (Fiebig et al., 2021) (‰)
5	0.651	0.004	0.660	0.006	0.656	0.273	0.019	0.273	0.011	0.276
10	0.636	0.007	0.634	0.008	0.640	0.260	0.021	0.265	0.006	0.268
15	0.626	0.008	0.628	0.01	0.625	0.259	0.011	0.256	0.008	0.261
25	0.594	0.008	0.603	0.006	0.595	0.250	0.010	0.251	0.008	0.247
30			0.577	0.006	0.581			0.236	0.012	0.241
35			0.563	0.007	0.568			0.242	0.007	0.235
65			0.508	0.011	0.496			0.212	0.011	0.207

Note. Values from Swart et al. (2021) are from inorganic calcite precipitations from 5°C to 65°C. Fiebig et al. (2021) values were calculated from a regression including lake and cave calcite, inorganic precipitations, and samples equilibrated at high temperature, with samples having crystallization temperatures from 7.9°C to 1,100°C.

the DIC pool has not achieved equilibrium (Guo, 2020; Tripati et al., 2015), and we find that our measured Δ_{47} values for samples precipitated at pH 10.5 have Δ_{47} that are elevated by 0.168–0.198‰ from mineral equilibrium values (Figure 3). While these observations are consistent with larger kinetic effects associated with CO_2 absorption, it is also likely that they include a kinetic contribution from growth rate effects.

For samples from this study and most from Tang et al. (2014) at pH 8.3, we find that Δ_{47} and Δ_{48} values are indistinguishable from equilibrium values irrespective of precipitation rate. This is the case for calcite precipitation at temperatures of 5 and 25°C, both with and without CA. This suggests that the intrinsic kinetic fractionation factor for clumped isotopes is close to unity (Guo, 2020) and that accurate temperatures can be retrieved even when there are large kinetic oxygen isotope effects. At higher pH, over the growth rates observed here, experimental data and modeling suggest that mineral disequilibrium occurs. Specifically, our calculations (Figure 8) suggest that samples precipitated at the same pH and temperature but at different growth rates, in a system where CO_2 absorption is dominant, and a DIC pool that has not reached equilibrium, may yield calcite with mineral disequilibrium of up to ~20 for $1000\ln(\alpha_{\text{calcite-water}})$, ~0.3‰ for Δ_{47}, and ~−0.6‰ for Δ_{48}. These effects are the largest for calcite growing at pH ≥ 9.5 and low temperature.

4.2. Equilibrium Clumped Isotope Compositions

Samples grown at pH 8.3 and at variable temperatures with CA yield Δ_{47} and Δ_{48} values that are consistent with mineral equilibrium as constrained using multiple independent approaches. The calcite growth rates achieved are ones that our modeling indicates should attain the equilibrium limit, and experimental data and model calculations converge (Figure 8). Additionally, our equilibrium samples were compared to previously published equilibrium Δ_{47} and Δ_{48} values (Table 5).

These results lend further support to experimental and field-derived calibration data sets being in quasi-equilibrium. An *F* test (performed in PRISM 7) was used for a statistical comparison between experimentally determined regressions for Δ_{47}-Δ_{48} values for equilibrium samples with known precipitation temperatures from Swart et al. (2021), Fiebig et al. (2021), and this study (Table 6). The test determined that the regressions were not statistically different ($p = 0.99$, Table 6) and a combined regression is represented by Equation 12 (Figure 10).

$$\Delta_{47\ \text{I-CDES}} = (2.430 \pm 0.117)\ \Delta_{48\ \text{CDES 90}} - (0.006 \pm 0.029);\ r^2 = 0.96 \quad (12)$$

The data from Fiebig et al. (2021) includes lake and cave calcites, inorganic precipitations, and samples equilibrated at high temperatures, with samples having crystallization temperatures from 7.9 to 1,100°C. Sample data from Swart et al. (2021) include 7 inorganic calcite precipitations from 5 to 65°C (Table 5).

It was also determined that the experimental regressions based on samples with known precipitation temperatures from Swart et al. (2021), Fiebig et al. (2021), and this study are statistically indistinguishable ($p > 0.99$) from the Δ_{47}-Δ_{48} regression from Lucarelli, Carroll, et al. (2023), which is based on measurements of 20 quasi-equilibrium

Table 6
Extra Sum-of-Squares F Test Results, Which Determine if Regressions Are Significantly Different and If All Data Sets Can Be Represented by One Combined Regression

Comparison of fits	Source of regression	Null hypothesis	Alternative hypothesis	P Value	Conclusion (alpha = 0.05)	Preferred model	F (DFn, DFd)
Δ_{47} versus Δ_{48}	Swart et al. (2021), Fiebig et al. (2021), this study	One curve for all data sets	Different curve for each data set	0.99	Do not reject null hypothesis	One curve for all data sets	0.03 (6, 43)
Δ_{47} versus Δ_{48}	Swart et al. (2021), Fiebig et al. (2021), Lucarelli, Carroll, et al. (2023), this study	One curve for all data sets	Different curve for each data set	>0.99	Do not reject null hypothesis	One curve for all data sets	0.05 (8, 57)
Δ_{47} versus 10^6 T^{-2}	Swart et al. (2021), Fiebig et al. (2021), this study	One curve for all data sets	Different curve for each data set	0.99	Do not reject null hypothesis	One curve for all data sets	0.13 (6, 43)
Δ_{48} versus 10^6 T^{-2}	Swart et al. (2021), Fiebig et al. (2021), this study	One curve for all data sets	Different curve for each data set	0.99	Do not reject null hypothesis	One curve for all data sets	0.03 (6, 43)

Note. Experimental regressions for samples with known precipitation temperature were used from Swart et al. (2021), Fiebig et al. (2021), and this study. An additional comparison was performed using an experimental Δ_{47}-Δ_{48} regression with samples of unknown precipitation temperature, including standards, from Lucarelli, Carroll, et al. (2023).

samples including standards. The combined regression for these experimental data sets is represented by Equation 13.

$$\Delta_{47\ \text{I-CDES}} = (2.318 \pm 0.071)\ \Delta_{48\ \text{CDES 90}} + (0.019 \pm 0.018);\ r^2 = 0.97 \quad (13)$$

An F test was used to test for statistical differences between experimentally determined regressions for Δ_{47}-10^6T^{-2} and Δ_{48}-10^6T^{-2} from Swart et al. (2021), Fiebig et al. (2021), and this study (Figure 10 and Table 6). It was determined that these regressions were not statistically different ($p = 0.99$ for Δ_{47} vs. 10^6T^{-2}; $p = 0.99$ for Δ_{48} vs. 10^6T^{-2}). The combined regressions are presented in Equations 14 and 15 with temperature in Kelvin.

$$\Delta_{47\ \text{I-CDES}} = (0.037\ \pm 0.001) \times 10^6\ T^{-2} + (0.178\ \pm 0.009);\ r^2 = 0.99 \quad (14)$$

$$\Delta_{48\ \text{CDES 90}} = (0.015 \pm 0.001) \times 10^6\ T^{-2} + (0.078 \pm 0.006);\ r^2 = 0.98 \quad (15)$$

Small offsets in Δ_{47} and Δ_{48} are likely from differences in standardization. This study and Lucarelli, Carroll, et al. (2023) used carbonate-based standardization, Swart et al. (2021) used gas-based standardization, and Fiebig et al. (2021) presented data normalized to both carbonate- and gas-based standardization. For Δ_{47}, this study used the I-CDES reference frame, while Swart et al. (2021) and Fiebig et al. (2021) used the CDES 90 reference frame. While I-CDES and CDES 90 should produce identical data given adequate standardization, as they both present data at 90°C, the I-CDES reference frame uses multi-lab determined values presented in Bernasconi et al. (2021) for the carbonate standards ETH-1, ETH-2, and ETH-3 for standardization, while CDES 90 may use slightly different values for these carbonate standards and other carbonate standards or may also present data relative to equilibrated gas standards. All Δ_{48} data reported thus far uses the CDES 90 reference frame; however, differences in values used for carbonate standards and the use of carbonate and/or gas-based standardization vary between labs, as discussed in Lucarelli, Carroll, et al. (2023). Additionally, Δ_{48} is relatively sensitive compared to Δ_{47} to subtle changes in transfer functions and nonlinearity slopes used in data corrections. For example, a shift of ~0.05 in the slope of the Δ_{48} transfer function can shift Δ_{48} values by ~0.029‰, while the same magnitude shift in the Δ_{47} transfer function will shift Δ_{47} values by ~0.013‰ (Table S3, see the Data Availability Statement). Despite this, the consistency of the equilibrium regressions from this work and previous studies supports the use of carbonate standards for calculating unknown Δ_{48}.

4.3. Identifying Sources of Disequilibrium and Extracting Primary Temperatures Using Dual Clumped Isotopes

Our results may be relevant to clumped or oxygen isotope based temperature reconstructions, or $\delta^{18}O_{water}$ estimates, using biominerals that precipitate in the presence of CA including coccolithophores (Nimer et al., 1994;

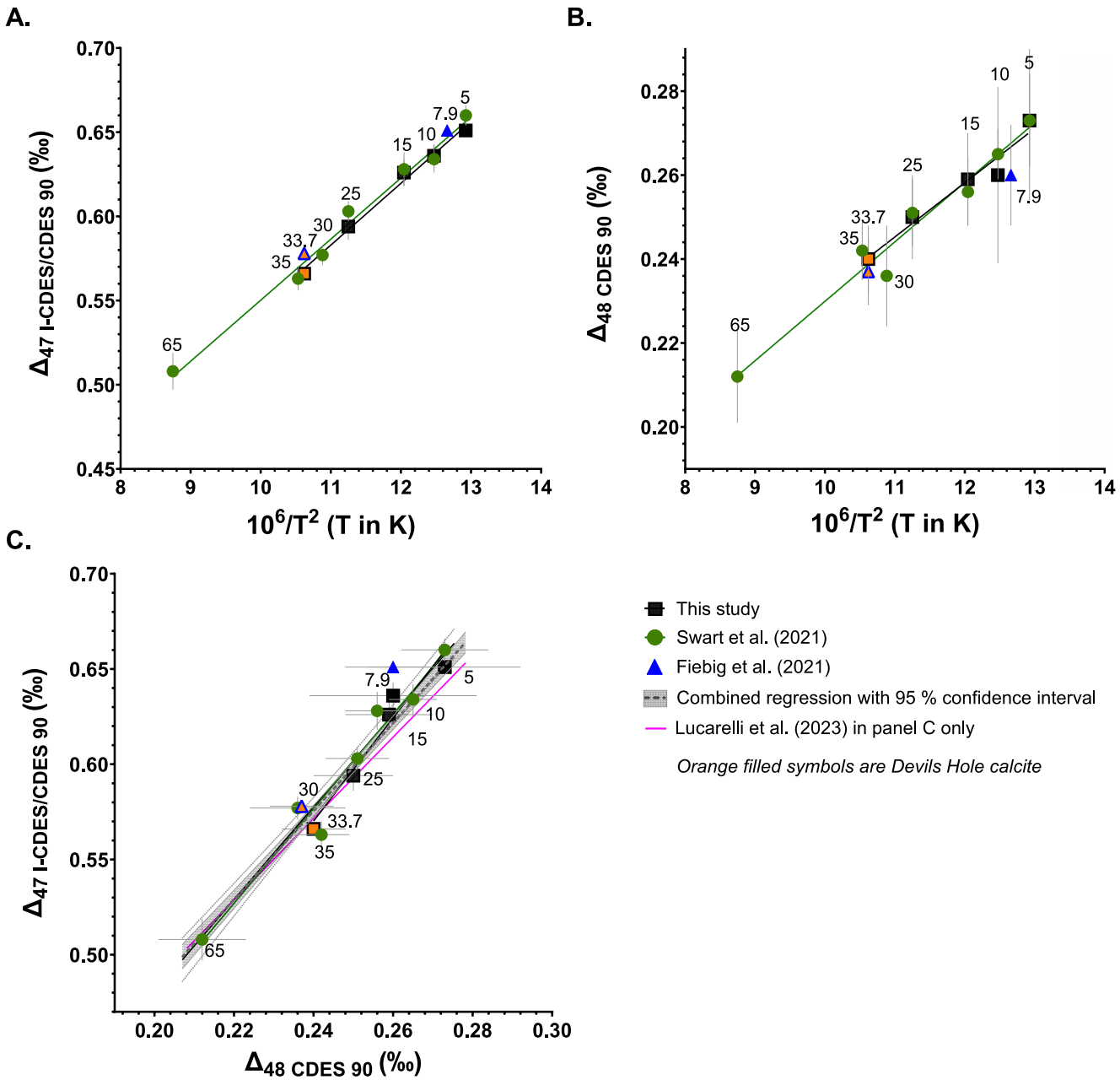

Figure 10. Comparison of quasi-equilibrium Δ_{47} and Δ_{48} values from calcite with well constrained precipitation temperatures from this work and previously published results, with (a) Δ_{47}-10^6 T^{-2}, (b) Δ_{48}-10^6 T^{-2}, and (c) Δ_{47}-Δ_{48}. The results from this study are for calcite precipitated at pH 8.3 with CA. In panels (a, b), results from this study are compared to results from Swart et al. (2021), based on calcite from precipitation experiments, and Fiebig et al. (2021), based on cave calcite and equilibrated calcite. In panel (c), results from Lucarelli, Carroll, et al. (2023) are shown, which is a regression (pink line in panel c) based on quasi-equilibrium carbonates with mostly unknown precipitation temperatures. All regressions were determined to be statistically indistinguishable, and combined regressions were determined (Equations 12–15). The symbols with orange fill indicate Devils Hole calcite, which has a constrained precipitation temperature of 33.7 ± 0.2°C (Plummer et al., 2000). Numbers by symbols indicate precipitation temperature in Celsius. Error bars indicate 1 SE.

Soto et al., 2006), other phytoplankton (Rost et al., 2003), oysters (Miyamoto et al., 1996; Yu et al., 2006), coral (Al-Horani et al., 2003; Bertucci et al., 2011; Kurman et al., 2017; Moya et al., 2008; Weis et al., 1989), and benthic foraminifera (de Goeyse et al., 2019). We show that varying [CA] affects the covariation and equilibration time for oxygen and dual clumped isotope values, building on results from previous work (Thaler et al., 2020; Tripati et al., 2015; Watkins et al., 2013).

Other dual clumped isotope studies have suggested that it may be possible to reconstruct temperature from samples that formed under disequilibrium conditions (Bajnai et al., 2020; Davies et al., 2022, 2023; Guo, 2020). This work supports this approach for samples formed at high pH, as we have calculated linear regressions at varying pH and temperature that could potentially correct for KIEs from hydration and hydroxylation. However, extra care should be taken with biominerals that precipitated in the presence of CA, as this work also indicates that [CA] has a significant effect on the expression of KIEs (Figure 3). We observed significantly different kinetic slopes for samples precipitated in the presence of CA versus samples precipitated without CA (Figure 7). Considering that organisms used for temperature reconstructions may have varying [CA] (Al-Horani et al., 2003; Bertucci et al., 2011; de Goeyse et al., 2019; Miyamoto et al., 1996; Moya et al., 2008; Nimer et al., 1994; Rost et al., 2003; Soto et al., 2006; Yu et al., 2006), this could result in the necessity of species-specific corrections to extract primary precipitation temperature.

5. Conclusions

We produced quasi-equilibrium Δ_{47}, Δ_{48}, and $\delta^{18}O$ values by precipitating calcite at 5°C, 10°C, 15°C, and 25°C at pH 8.3 with the enzyme CA. This data provides an independent set of constraints on the equilibrium relationship between Δ_{47}-Δ_{48}, Δ_{47}-T, Δ_{48}-T, Δ_{47}-$\delta^{18}O$, and Δ_{48}-$\delta^{18}O$. The experimentally determined equilibrium Δ_{47}-Δ_{48} regression from this study is statistically indistinguishable from published data sets. We report a combined equilibrium regression fit through all experimental data from Swart et al. (2021), Fiebig et al. (2021), Lucarelli, Carroll, et al. (2023), and this study.

From our experiments at elevated pH, we observe enriched Δ_{47} values and depleted Δ_{48} and $\delta^{18}O$, relative to equilibrium. The largest Δ_{47} enrichment observed was 0.203‰ at pH 10.5 and 5°C. The largest Δ_{48} depletion was −0.693‰ at pH 11 and 5°C. Calcite precipitated at pH ≥ 9.5 had Δ_{48} values less than 0‰, indicating anti-clumped values (less than a stochastic distribution). Calcite precipitated with CA had reduced Δ_{47} and Δ_{48} kinetic effects, where CA was more efficient at catalyzing Δ_{48} than Δ_{47}. The Δ_{47}/Δ_{48} kinetic slopes differed for calcite precipitated at pH ≥ 9.5 without CA relative to calcite precipitated at pH ≥ 9.5 with CA. Calcite precipitated at pH ≤ 9.0 had negligible clumped isotope kinetic effects, while kinetic oxygen isotope effects may have been present.

The observed clumped isotope values in calcite samples grown at elevated pH without CA can be explained by hydration/hydroxylation during CO_2 absorption. Calcite precipitated at fast growth rates may inherit larger kinetic isotopic effects from CO_2 hydration/hydroxylation and a disequilibrium DIC pool compared to calcite precipitated at slower growth rates. KIEs associated with fast growth rates and CO_2 hydration/hydroxylation may be as large as +0.2‰ for Δ_{47} and −0.7‰ for Δ_{48}.

Conflict of Interest

The authors declare no conflicts of interest relevant to this study.

Data Availability Statement

Sample and standard replicate data, and XRD data are available at the data repository figshare (Lucarelli et al., 2025).

Acknowledgments

We thank lab members past and present for their work running standards, efforts in data entry, and contributions to discussions, including Ben Elliott, Emily McFerson, Robert Ulrich, and Ka'ron Marshall. We thank the NAWI Graz Central Lab for Water, Minerals and Rocks for experimental and analytical support, and Albrecht Leis (JR-AquaConSol, Graz) for support on liquid isotope analyses. This work was funded by DOE BES grant DE-FG02-83613ER16402 and Heising-Simons Foundation Grant 2022-3314 to Aradhna Tripati. Jamie Lucarelli and Zeeshan Parvez also acknowledge support from fellowships granted by The Center for Diverse Leadership in Science supported by the Packard Foundation, Sloan Foundation, Silicon Valley Community Foundation, and NSF (ICER-2039462 for Veterans in STEM). Jamie Lucarelli received support from Cota Robles and Dissertation Year Fellowships from the University of California, Los Angeles, and Zeeshan Parvez received support as a Tillman Scholar. AT initiated and supported the work. AT, MD, BP, and JL designed the research. BP carried out the precipitation experiments with input from MD and JL. JL performed the isotope analyses and calculations with input from AT. ZP and JL contributed to the box model and IsoDIC calculations. JW provided the box model script. JL, BP, RE, MD, and AT contributed insights to data analyses and interpretations. JL wrote the manuscript with guidance from AT and input from all coauthors. AT and RE advised JL and ZP.

References

Adkins, J. F., Boyle, E. A., Curry, W. B., & Lutringer, A. (2003). Stable isotopes in deep-sea corals and a new mechanism for "vital effects.". *Geochimica et Cosmochimica Acta*, *67*(6), 1129–1143. https://doi.org/10.1016/s0016-7037(02)01203-6

Al-Horani, F. A., Al-Moghrabi, S. M., & de Beer, D. (2003). Microsensor study of photosynthesis and calcification in the scleractinian coral, galaxea fascicularis: Active internal carbon cycle. *Journal of Experimental Marine Biology and Ecology*, *288*, 1–15. https://doi.org/10.1016/s0022-0981(02)00578-6

Anagnostou, E., Huang, K.-F., You, C.-F., Sikes, E. L., & Sherrell, R. M. (2012). Evaluation of boron isotope ratio as a pH proxy in the deep sea coral desmophyllum dianthus: Evidence of physiological pH adjustment. *Earth and Planetary Science Letters*, *349–350*, 251–260. https://doi.org/10.1016/j.epsl.2012.07.006

Bajnai, D., Coplen, T. B., Methner, K., Löffler, N., Krsnik, E., & Fiebig, J. (2021). Devils hole calcite was precipitated at ±1 C stable aquifer temperatures during the last half million years. *Geophysical Research Letters*, *48*(11), e2021GL093257. https://doi.org/10.1029/2021gl093257

Bajnai, D., Guo, W., Spötl, C., Coplen, T. B., Methner, K., Löffler, N., et al. (2020). Dual clumped isotope thermometry resolves kinetic biases in carbonate formation temperatures. *Nature Communications*, *11*(1), 4005. https://doi.org/10.1038/s41467-020-17501-0

Beck, W. C., Grossman, E. L., & Morse, J. W. (2005). Experimental studies of oxygen isotope fractionation in the carbonic acid system at 15°, 25°, and 40°C. *Geochimica et Cosmochimica Acta*, *69*(14), 3493–3503. https://doi.org/10.1016/j.gca.2005.02.003

Berg, J., Tymoczko, J., & Stryer, L. (2002). *Biochemistry* (5th ed.). W. H. Freeman.

Bernasconi, S. M., Daëron, M., Bergmann, K. D., Bonifacie, M., Meckler, A. N., Affek, H. P., et al. (2021). InterCarb: A community effort to improve interlaboratory standardization of the carbonate clumped isotope thermometer using carbonate standards. *Geochemistry, Geophysics, Geosystems*, *22*(5), e2020GC009588. https://doi.org/10.1029/2020gc009588

Bernasconi, S. M., Müller, I. A., Bergmann, K. D., Breitenbach, S. F. M., Fernandez, A., Hodell, D. A., et al. (2018). Reducing uncertainties in carbonate clumped isotope analysis through consistent carbonate-based standardization. *Geochemistry, Geophysics, Geosystems*, *19*(9), 2895–2914. https://doi.org/10.1029/2017GC007385

Bernecker, M., Hofmann, S., Staudigel, P. T., Davies, A. J., Tagliavento, M., Meijer, N., et al. (2023). A robust methodology for triple (Δ47,Δ48, Δ49) clumped isotope analysis of carbonates. *Chemical Geology*, *642*, 121803. https://doi.org/10.1016/j.chemgeo.2023.121803

Bertucci, A., Innocenti, A., Scozzafava, A., Tambutté, S., Zoccola, D., & Supuran, C. T. (2011). Carbonic anhydrase inhibitors. Inhibition studies with anions and sulfonamides of a new cytosolic enzyme from the scleractinian coral Stylophora pistillata. *Bioorganic & Medicinal Chemistry Letters*, *21*(2), 710–714. https://doi.org/10.1016/j.bmcl.2010.11.124

Boettger, J. D., & Kubicki, J. D. (2021). Equilibrium and kinetic isotopic fractionation in the CO_2 hydration and hydroxylation reactions: Analysis of the role of hydrogen-bonding via quantum mechanical calculations. *Geochimica et Cosmochimica Acta*, *292*, 37–63. https://doi.org/10.1016/j.gca.2020.09.019

Brand, W. A., Assonov, S. S., & Coplen, T. B. (2010). Correction for the ^{17}O interference in $\delta(^{13}C)$ measurements when analyzing CO_2 with stable isotope mass spectrometry (IUPAC technical report). *Pure and Applied Chemistry*, *82*(8), 1719–1733. https://doi.org/10.1351/pac-rep-09-01-05

Chen, S., Gagnon, A. C., & Adkins, J. F. (2018). Carbonic anhydrase, coral calcification and a new model of stable isotope vital effects. *Geochimica et Cosmochimica Acta*, *236*, 179–197. https://doi.org/10.1016/j.gca.2018.02.032

Christensen, J. N., Watkins, J. M., Devriendt, L. S., DePaolo, D. J., Conrad, M. E., Voltolini, M., et al. (2021). Isotopic fractionation accompanying CO_2 hydroxylation and carbonate precipitation from high pH waters at the Cedars, California, USA. *Geochimica et Cosmochimica Acta*, *301*, 91–115. https://doi.org/10.1016/j.gca.2021.01.003

Coplen, T. B. (2007). Calibration of the calcite-water oxygen-isotope geothermometer at Devils Hole, Nevada, a natural laboratory. *Geochimica et Cosmochimica Acta*, *71*(16), 3948–3957. https://doi.org/10.1016/j.gca.2007.05.028

Daëron, M. (2021). Full propagation of analytical uncertainties in Δ47 measurements. *Geochemistry, Geophysics, Geosystems*, *22*(5), e2020GC009592. https://doi.org/10.1029/2020gc009592

Daëron, M., Blamart, D., Peral, M., & Affek, H. P. (2016). Absolute isotopic abundance ratios and the accuracy of Δ_{47} measurements. *Chemical Geology*, *442*, 83–96. https://doi.org/10.1016/j.chemgeo.2016.08.014

Daëron, M., Drysdale, R. N., Peral, M., Huyghe, D., Blamart, D., Coplen, T. B., et al. (2019). Most Earth-surface calcites precipitate out of isotopic equilibrium. *Nature Communications*, *10*(1), 429. https://doi.org/10.1038/s41467-019-08336-5

Daëron, M., Guo, W., Eiler, J., Genty, D., Blamart, D., Boch, R., et al. (2011). 13C18O clumping in speleothems: Observations from natural caves and precipitation experiments. *Geochimica et Cosmochimica Acta*, *75*(12), 3303–3317. https://doi.org/10.1016/j.gca.2010.10.032

Davies, A. J., Brand, U., Tagliavento, M., Bitner, M. A., Bajnai, D., Staudigel, P., et al. (2023). Isotopic disequilibrium in brachiopods disentangled with dual clumped isotope thermometry. *Geochimica et Cosmochimica Acta*, *359*, 135–147. https://doi.org/10.1016/j.gca.2023.08.005

Davies, A. J., Guo, W., Bernecker, M., Tagliavento, M., Raddatz, J., Gischler, E., et al. (2022). Dual clumped isotope thermometry of coral carbonate. *Geochimica et Cosmochimica Acta*, *338*, 66–78. https://doi.org/10.1016/j.gca.2022.10.015

de Goeyse, S., Webb, A. E., Reichart, G.-J., & de Nooijer, L. J. (2019). Carbonic anhydrase is involved in calcification by the benthic foraminifer Amphistegina lessonii. *Biogeosciences*, *18*(2), 393–401. https://doi.org/10.5194/bg-18-393-2021

Defliese, W. F., & Tripati, A. (2020). Analytical effects on clumped isotope thermometry: Comparison of a common sample set analyzed using multiple instruments, types of standards, and standardization windows. *Rapid Communications in Mass Spectrometry*, *34*(8), e8666. https://doi.org/10.1002/rcm.8666

Dennis, K. J., Affek, H. P., Passey, B. H., Schrag, D. P., & Eiler, J. M. (2011). Defining an absolute reference frame for "clumped" isotope studies of CO_2. *Geochimica et Cosmochimica Acta*, *75*(22), 7117–7131. https://doi.org/10.1016/j.gca.2011.09.025

DePaolo, D. J. (2011). Surface kinetic model for isotopic and trace element fractionation during precipitation of calcite from aqueous solutions. *Geochimica et Cosmochimica Acta*, *75*(4), 1039–1056. https://doi.org/10.1016/j.gca.2010.11.020

Dietzel, M., Gussone, N., & Eisenhauer, A. (2004). Co-precipitation of Sr^{2+} and Ba^{2+} with aragonite by membrane diffusion of CO_2 between 10 and 50°C. *Chemical Geology*, *203*(1–2), 139–151. https://doi.org/10.1016/j.chemgeo.2003.09.008

Dietzel, M., Tang, J., Leis, A., & Köhler, S. J. (2009). Oxygen isotopic fractionation during inorganic calcite precipitation—effects of temperature, precipitation rate and pH. *Chemical Geology*, *268*(1–2), 107–115. https://doi.org/10.1016/j.chemgeo.2009.07.015

Dietzel, M., & Usdowski, E. (1996). Coprecipitation of Ni^{2+}, Co^{2+}, and Mn^{2+} with galena and covellite, and of Sr^{2+} with calcite during crystallization via diffusion of H_2S and CO_2 through polyethylene at 20°C: Power law and Nernst law control of trace element partitioning. *Chemical Geology*, *131*(1–4), 55–65. https://doi.org/10.1016/0009-2541(96)00026-5

Douglas, P. M., Stolper, D. A., Eiler, J. M., Sessions, A. L., Lawson, M., Shuai, Y., et al. (2017). Methane clumped isotopes: Progress and potential for a new isotopic tracer. *Organic Geochemistry*, *113*, 262–282. https://doi.org/10.1016/j.orggeochem.2017.07.016

Eagle, R. A., Guillermic, M., De Corte, I., Alvarez Caraveo, B., Bove, C. B., Misra, S., et al. (2022). Physicochemical control of Caribbean coral calcification linked to host and symbiont responses to varying pCO_2 and temperature. *Journal of Marine Science and Engineering*, *10*(8), 1075. https://doi.org/10.3390/jmse10081075

Eiler, J. M., & Schauble, E. (2004). $^{18}O^{13}C^{16}O$ in Earth's atmosphere. *Geochimica et Cosmochimica Acta*, *68*(23), 4767–4777. https://doi.org/10.1016/j.gca.2004.05.035

Fiebig, J., Bajnai, D., Löffler, N., Methner, K., Krsnik, E., Mulch, A., & Hofmann, S. (2019). Combined high-precision Δ_{48} and Δ_{47} analysis of carbonates. *Chemical Geology*, *522*, 186–191.

Fiebig, J., Daëron, M., Bernecker, M., Guo, W., Schneider, G., Boch, R., et al. (2021). Calibration of the dual clumped isotope thermometer for carbonates. *Geochimica et Cosmochimica Acta*, *312*, 235–256. https://doi.org/10.1016/j.gca.2021.07.012

Ghosh, P., Adkins, J., Affek, H., Balta, B., Guo, W., Schauble, E. A., et al. (2006). ^{13}C–^{18}O bonds in carbonate minerals: A new kind of paleothermometer. *Geochimica et Cosmochimica Acta*, *70*(6), 1439–1456. https://doi.org/10.1016/j.gca.2005.11.014

Griffiths, M. L., Eagle, R. A., Kim, S. L., Flores, R. J., Becker, M. A., Maisch IV, H. M., et al. (2023). Endothermic physiology of extinct megatooth sharks. *Proceedings of the national academy of sciences* (Vol. 120(27), p. e2218153120). https://doi.org/10.1073/pnas.2218153120

Guo, W. (2020). Kinetic clumped isotope fractionation in the DIC-H_2O-CO_2 system: Patterns, controls, and implications. *Geochimica et Cosmochimica Acta*, *268*, 230–257. https://doi.org/10.1016/j.gca.2019.07.055

Guo, Y., Deng, W., & Wei, G. (2019). Kinetic effects during the experimental transition of aragonite to calcite in aqueous solution: Insights from clumped and oxygen isotope signatures. *Geochimica et Cosmochimica Acta*, *248*, 210–230. https://doi.org/10.1016/j.gca.2019.01.012

Hill, P. S., Schauble, E. A., & Tripati, A. (2020). Theoretical constraints on the effects of added cations on clumped, oxygen, and carbon isotope signatures of dissolved inorganic carbon species and minerals. *Geochimica et Cosmochimica Acta*, *269*, 496–539. https://doi.org/10.1016/j.gca.2019.10.016

Hill, P. S., Tripati, A. K., & Schauble, E. A. (2014). Theoretical constraints on the effects of pH, salinity, and temperature on clumped isotope signatures of dissolved inorganic carbon species and precipitating carbonate minerals. *Geochimica et Cosmochimica Acta*, *125*, 610–652. https://doi.org/10.1016/j.gca.2013.06.018

Huntington, K. W., Eiler, J. M., Affek, H. P., Guo, W., Bonifacie, M., Yeung, L. Y., et al. (2009). Methods and limitations of "clumped" CO2 isotope (Δ47) analysis by gas-source isotope ratio mass spectrometry. *Journal of Mass Spectrometry*, *44*(9), 1318–1329. https://doi.org/10.1002/jms.1614

John, C. M., & Bowen, D. (2016). Community software for challenging isotope analysis: First applications of "Easotope" to clumped isotopes. *Rapid Communications in Mass Spectrometry*, *30*(21), 2285–2300. https://doi.org/10.1002/rcm.7720

Johnson, K. S. (1982). Carbon dioxide hydration and dehydration kinetics in seawater 1: CO_2 reaction kinetics. *Limnology & Oceanography*, *27*(5), 849–855. https://doi.org/10.4319/lo.1982.27.5.0849

Kernohan, J. C. (1964). The activity of bovine carbonic anhydrase in imidazole buffers. *Biochimica et Biophysica Acta (BBA)-Specialized Section on Enzymological Subjects*, *81*(2), 346–356. https://doi.org/10.1016/0926-6569(64)90050-1

Kim, S. T., & O'Neil, J. R. (1997). Equilibrium and nonequilibrium oxygen isotope effects in synthetic carbonates. *Geochimica et Cosmochimica Acta*, *61*(16), 3461–3475. https://doi.org/10.1016/s0016-7037(97)00169-5

Kimball, J., Eagle, R., & Dunbar, R. (2016). Carbonate "clumped" isotope signatures in aragonitic scleractinian and calcitic gorgonian deep-sea corals. *Biogeosciences*, *13*(23), 6487–6505. https://doi.org/10.5194/bg-13-6487-2016

Knoche, W. (1980). Chemical reactions of CO_2 in water. In C. Bauer, G. Gros, & H. Bartels (Eds.), *Biophysics and physiology of carbon dioxide, proceedings in life sciences* (pp. 3–11). Springer Berlin Heidelberg.

Kurman, M., Gómez, C. E., Georgian, S. E., Lunden, J. J., & Cordes, E. E. (2017). Seawater carbon chemistry and calcification, carbonic anhydrase activity of cold-water coral Lophelia Pertusa.

Liu, Y. W., Sutton, J. N., Ries, J. B., & Eagle, R. A. (2020). Regulation of calcification site pH is a polyphyletic but not always governing response to ocean acidification. *Science Advances*, *6*(5), eaax1314. https://doi.org/10.1126/sciadv.aax1314

Lucarelli, J., Purgstaller, B., Parvez, Z., Watkins, J. M., Eagle, R., Dietzel, M., & Tripati, A. (2025). Dual clumped isotope (Δ_{47}, Δ_{48}) values for calcite grown at varying pH and carbonic anhydrase concentrations constrain calcite equilibrium and kinetic isotope effects [Dataset]. *Figshare*. https://doi.org/10.6084/m9.figshare.28237589.v3

Lucarelli, J. K., Carroll, H. M., Ulrich, R. N., Elliott, B. M., Coplen, T. B., Eagle, R. A., & Tripati, A. (2023). Equilibrated gas and carbonate standard-derived dual (Δ_{47} and Δ_{48}) clumped isotope values. *Geochemistry, Geophysics, Geosystems*, *24*(2), 2022GC010458. https://doi.org/10.1029/2022gc010458

Lucarelli, J. K., Purgstaller, B., Ulrich, R. N., Parvez, Z., Leis, A., Goetschl, K. E., et al. (2023). Dual clumped (Δ_{47}-Δ_{48}) isotope data for amorphous carbonates and transformation products reveal a novel mechanism for disequilibrium clumped isotope effects. *Geochimica et Cosmochimica Acta*, *359*, 119–134. https://doi.org/10.1016/j.gca.2023.07.027

McConnaughey, T. (1989). ^{13}C and ^{18}O isotopic disequilibrium in biological carbonates: II. In vitro simulation of kinetic isotope effects. *Geochimica et Cosmochimica Acta*, *53*(1), 163–171. https://doi.org/10.1016/0016-7037(89)90283-4

Meckler, A. N., Ziegler, M., Millán, M. I., Breitenbach, S. F., & Bernasconi, S. M. (2014). Long-term performance of the Kiel carbonate device with a new correction scheme for clumped isotope measurements. *Rapid Communications in Mass Spectrometry*, *28*(15), 1705–1715. https://doi.org/10.1002/rcm.6949

Merritt, D. A., & Hayes, J. M. (1994). Factors controlling precision and accuracy in isotope-ratio-monitoring mass spectrometry. *Analytical Chemistry*, *66*(14), 2336–2347. https://doi.org/10.1021/ac00086a020

Miller, R. F., Berkshire, D. C., Kelley, J. J., & Hood, D. W. (1971). Method for determination of reaction rates of carbon dioxide with water and hydroxyl ion in seawater. *Environmental Science & Technology*, *5*(2), 127–133. https://doi.org/10.1021/es60049a006

Miyamoto, H., Miyashita, T., Okushima, M., Nakano, S., Morita, T., & Matsushiro, A. (1996). A carbonic anhydrase from the nacreous layer in oyster pearls. *Proceedings of the national academy of sciences* (Vol. 93(18), pp. 9657–9660). https://doi.org/10.1073/pnas.93.18.9657

Moya, A., Tambutté, S., Bertucci, A., Tambutté, E., Lotto, S., Vullo, D., et al. (2008). Carbonic anhydrase in the scleractinian coral Stylophora pistillata. *Journal of Biological Chemistry*, *283*(37), 25475–25484. https://doi.org/10.1074/jbc.M804726200

Nimer, N. A., Guan, Q., & Merrett, M. J. (1994). Extra- and intra-cellular carbonic anhydrase in relation to culture age in a high-calcifying strain of Emiliania Huxleyi Lohmann. *New Phytologist*, *126*(4), 601–607. https://doi.org/10.1111/j.1469-8137.1994.tb02954.x

Paneth, P., & O'Leary, M. H. (1985). Carbon isotope effect on dehydration of bicarbonate ion catalyzed by carbonic anhydrase. *Biochemistry*, *24*(19), 5143–5147. https://doi.org/10.1021/bi00340a028

Parvez, Z. A., El-Shenawy, M. I., Lucarelli, J. K., Kim, S. T., Johnson, K. R., Wright, K., et al. (2024). Dual carbonate clumped isotope (Δ_{47}-Δ_{48}) measurements constrain different sources of kinetic isotope effects and quasi-equilibrium signatures in cave carbonates. *Geochimica et Cosmochimica Acta*, *366*, 95–112. https://doi.org/10.1016/j.gca.2023.11.017

Parvez, Z. A., Lucarelli, J. K., Matamoros, I. W., Rubi, J., Miguel, K., Elliott, B., et al. (2023). Dual carbonate clumped isotopes (Δ_{47}-Δ_{48}) constrains kinetic effects and timescales in peridotite-associated springs at the cedars, northern California. *Geochimica et Cosmochimica Acta*, *358*, 77–92. https://doi.org/10.1016/j.gca.2023.06.022

Passey, B. H., Levin, N. E., Cerling, T. E., Brown, F. H., & Eiler, J. M. (2010). High-temperature environments of human evolution in East Africa based on bond ordering in Paleosol carbonates. *Proceedings of the national academy of sciences* (Vol. 107(25), pp. 11245–11249). https://doi.org/10.1073/pnas.1001824107

Petersen, S. V., & Schrag, D. P. (2014). Clumped isotope measurements of small carbonate samples using a high-efficiency dual-reservoir technique. *Rapid Communications in Mass Spectrometry*, *28*(21), 2371–2381. https://doi.org/10.1002/rcm.7022

Plummer, L. N., Busenberg, E., & Riggs, A. C. (2000). In-situ growth of calcite at Devils Hole, Nevada: Comparison of field and laboratory rates to a 500,000 year record of near-equilibrium calcite growth. *Aquatic Geochemistry*, *6*(2), 257–274. https://doi.org/10.1023/a:1009627710476

Rost, B., Riebesell, U., Burkhardt, S., & Sültemeyer, D. (2003). Carbon acquisition of Bloom-forming marine phytoplankton. *Limnology & Oceanography*, *48*(1), 55–67. https://doi.org/10.4319/lo.2003.48.1.0055

Saenger, C., Affek, H. P., Felis, T., Thiagarajan, N., Lough, J. M., & Holcomb, M. (2012). Carbonate clumped isotope variability in shallow water corals: Temperature dependence and growth-related vital effects. *Geochimica et Cosmochimica Acta*, *99*, 224–242. https://doi.org/10.1016/j.gca.2012.09.035

Schauble, E. A., Ghosh, P., & Eiler, J. M. (2006). Preferential formation of ^{13}C-^{18}O bonds in carbonate minerals, estimated using first-principles lattice dynamics. *Geochimica et Cosmochimica Acta*, *70*(10), 2510–2529. https://doi.org/10.1016/j.gca.2006.02.011

Soto, A. R., Zheng, H., Shoemaker, D., Rodriguez, J., Read, B. A., & Wahlund, T. M. (2006). Identification and preliminary characterization of two cDNAs encoding unique carbonic anhydrases from the marine alga Emiliania Huxleyi. *Applied and Environmental Microbiology*, *72*(8), 5500–5511. https://doi.org/10.1128/aem.00237-06

Spooner, P. T., Guo, W., Robinson, L. F., Thiagarajan, N., Hendry, K. R., Rosenheim, B. E., & Leng, M. J. (2016). Clumped isotope composition of cold-water corals: A role for vital effects? *Geochim. Cosmochim.Acta*, *179*, 123–141. https://doi.org/10.1016/j.gca.2016.01.023

Staudigel, P., Davies, A. J., Bernecker, M., Tagliavento, M., van der Lubbe, H. J. L., Nooitgedacht, C., et al. (2023). Fingerprinting kinetic isotope effects and diagenetic exchange reactions using fluid inclusion and dual-clumped isotope analysis. *Geochemistry, Geophysics, Geosystems*, *24*(2), e2022GC010766. https://doi.org/10.1029/2022gc010766

Staudigel, P. T., & Swart, P. K. (2018). A kinetic difference between ^{12}C- and ^{13}C-Bound oxygen exchange rates results in decoupled $\delta^{18}O$ and Δ_{47} values of equilibrating DIC solutions. *Geochemistry, Geophysics, Geosystems*, *19*(8), 2371–2383. https://doi.org/10.1029/2018gc007500

Swart, P. K., Lu, C., Moore, E. W., Smith, M. E., Murray, S. T., & Staudigel, P. T. (2021). A calibration equation between Δ_{48} values of carbonate and temperature. *Rapid Communications in Mass Spectrometry*, *35*(17), e9147. https://doi.org/10.1002/rcm.9147

Tagliavento, M., Davies, A. J., Bernecker, M., Staudigel, P. T., Dawson, R. R., Dietzel, M., et al. (2023). Evidence for heterothermic endothermy and reptile-like eggshell mineralization in Troodon, a Non-avian maniraptoran theropod. *Proceedings of the National Academy of Sciences*, *120*(15), e2213987120. https://doi.org/10.1073/pnas.2213987120

Tang, J., Dietzel, M., Böhm, F., Köhler, S. J., & Eisenhauer, A. (2008). Sr^{2+}/Ca^{2+} and $^{44}Ca/^{40}Ca$ fractionation during inorganic calcite formation: II. Ca isotopes. *Geochimica et Cosmochimica Acta*, *72*, 3733–3745.

Tang, J., Dietzel, M., Fernandez, A., Tripati, A. K., & Rosenheim, B. E. (2014). Evaluation of kinetic effects on clumped isotope fractionation (Δ_{47}) during inorganic calcite precipitation. *Geochimica et Cosmochimica Acta*, *134*, 120–136. https://doi.org/10.1016/j.gca.2014.03.005

Thaler, C., Katz, A., Bonifacie, M., Ménez, B., & Ader, M. (2020). Oxygen isotope composition of waters recorded in carbonates in strong clumped and oxygen isotopic disequilibrium. *Biogeosciences*, *17*(7), 1731–1744. https://doi.org/10.5194/bg-17-1731-2020

Thiagarajan, N., Adkins, J., & Eiler, J. (2011). Carbonate clumped isotope thermometry of deep-sea corals and implications for vital effects. *Geochimica et Cosmochimica Acta*, *75*(16), 4416–4425. https://doi.org/10.1016/j.gca.2011.05.004

Tripati, A. K., Hill, P. S., Eagle, R. A., Mosenfelder, J. L., Tang, J., Schauble, E. A., et al. (2015). Beyond temperature: Clumped isotope signatures in dissolved inorganic carbon species and the influence of solution chemistry on carbonate mineral composition. *Geochimica et Cosmochimica Acta*, *166*, 344–371. https://doi.org/10.1016/j.gca.2015.06.021

Trotter, J., Montagna, P., McCulloch, M., Silenzi, S., Reynaud, S., Mortimer, G., et al. (2011). Quantifying the pH "vital effect" in the temperate zooxanthellate coral *Cladocora caespitosa*: Validation of the boron seawater pH proxy. *Earth and Planetary Science Letters*, *303*(3–4), 163–173. https://doi.org/10.1016/j.epsl.2011.01.030

Uchikawa, J., Chen, S., Eiler, J. M., Adkins, J. F., & Zeebe, R. E. (2021). Trajectory and timescale of oxygen and clumped isotope equilibration in the dissolved carbonate system under normal and enzymatically-catalyzed conditions at 25°C. *Geochimica et Cosmochimica Acta*, *314*, 313–333. https://doi.org/10.1016/j.gca.2021.08.014

Uchikawa, J., & Zeebe, R. E. (2012). The effect of carbonic anhydrase on the kinetics and equilibrium of the oxygen isotope exchange in the CO_2-H_2O system: Implications for $\delta^{18}O$ vital effects in biogenic carbonates. *Geochimica et Cosmochimica Acta*, *95*, 15–34. https://doi.org/10.1016/j.gca.2012.07.022

Upadhyay, D., Lucarelli, J., Arnold, A., Flores, R., Bricker, H., Ulrich, R. N., et al. (2021). Carbonate clumped isotope analysis (Δ_{47}) of 21 carbonate standards determined via gas-source isotope-ratio mass spectrometry on four instrumental configurations using carbonate-based standardization and multiyear data sets. *Rapid Communications in Mass Spectrometry*, *35*(17), e9143. https://doi.org/10.1002/rcm.9143

Usdowski, E., Michaelis, J., Boettcher, M., & Hoefs, J. (1991). Factors for the oxygen isotope equilibrium fractionation between aqueous and gaseous CO_2, carbonic acid, bicarbonate, carbonate, and water (19°C). *Zeitschrift für Physikalische Chemie (International Journal of Research in Physical Chemistry and Chemical Physics)*, *170*, 237–249.

Venn, A., Tambutté, E., Holcomb, M., Allemand, D., & Tambutté, S. (2011). Live tissue imaging shows reef corals elevate pH under their calcifying tissue relative to seawater. *PLoS One*, *6*(5), e20013. https://doi.org/10.1371/journal.pone.0020013

Venn, A. A., Tambutté, E., Crovetto, L., & Tambutté, S. (2025). pH regulation in coral photosymbiosis and calcification: A compartmental perspective. *New Phytologist*, *247*(2), 487–503. https://doi.org/10.1111/nph.70200

Wang, Z., Schauble, E. A., & Eiler, J. M. (2004). Equilibrium thermodynamics of multiply substituted isotopologues of molecular gases. *Geochimica et Cosmochimica Acta*, *68*(23), 4779–4797. https://doi.org/10.1016/j.gca.2004.05.039

Watkins, J., & Devriendt, L. (2022). A combined model for kinetic clumped isotope effects in the $CaCO_3$-DIC-H_2O system. *Geochemistry, Geophysics, Geosystems*, *23*(8), e2021GC010200. https://doi.org/10.1029/2021gc010200

Watkins, J. M., & Hunt, J. D. (2015). A process-based model for non-equilibrium clumped isotope effects in carbonates. *Earth and Planetary Science Letters*, *432*, 152–165. https://doi.org/10.1016/j.epsl.2015.09.042

Watkins, J. M., Hunt, J. D., Ryerson, F. J., & DePaolo, D. J. (2014). The influence of temperature, pH, and growth rate on the $\delta^{18}O$ composition of inorganically precipitated calcite. *Earth and Planetary Science Letters*, *404*, 332–343. https://doi.org/10.1016/j.epsl.2014.07.036

Watkins, J. M., Nielsen, L. C., Ryerson, F. J., & DePaolo, D. J. (2013). The influence of kinetics on the oxygen isotope composition of calcium carbonate. *Earth and Planetary Science Letters*, *375*, 349–360. https://doi.org/10.1016/j.epsl.2013.05.054

Weis, V. M., Smith, G. J., & Muscatine, L. (1989). A "CO_2 supply" mechanism in zooxanthellate cnidarians: Role of carbonic anhydrase. *Marine Biology*, *100*(2), 195–202. https://doi.org/10.1007/bf00391958

Weise, A., & Kluge, T. (2020). Isotope exchange rates in dissolved inorganic carbon between 40°C and 90°C. *Geochimica et Cosmochimica Acta*, *268*, 56–72. https://doi.org/10.1016/j.gca.2019.09.032

Winograd, I. J., Coplen, T. B., Landwehr, J. M., Riggs, A. C., Ludwig, K. R., Szabo, B. J., et al. (1992). Continuous 500,000-Year climate record from vein calcite in Devils Hole, Nevada. *Science*, *258*(5080), 255–260. https://doi.org/10.1126/science.258.5080.255

Winograd, I. J., Coplen, T. B., Szabo, B. J., & Riggs, A. C. (1988). A 250,000-Year climatic record from great basin vein calcite: Implications for milankovitch theory. *Science*, *242*(4883), 1275–1280. https://doi.org/10.1126/science.242.4883.1275

Yu, Z., Xie, L., Lee, S., & Zhang, R. (2006). A novel carbonic anhydrase from the mantle of the pearl oyster (*Pinctada fucata*). *Comparative Biochemistry and Physiology Part B: Biochemistry and Molecular Biology*, *143*(2), 190–194. https://doi.org/10.1016/j.cbpb.2005.11.006

Zeebe, R. E., & Wolf-Gladrow, D. A. (2001). *CO_2 in seawater: Equilibrium, kinetics, isotopes*. Elsevier Oceanography Series. Elsevier.

References From the Supporting Information

Wolthers, M., Nehrke, G., Gustafsson, J. P., & Van Cappellen, P. (2012). Calcite growth kinetics: Modeling the effect of solution stoichiometry. *Geochimica et Cosmochimica Acta*, *77*, 121–134. https://doi.org/10.1016/j.gca.2011.11.003

Zeebe, R. E. (2020). Oxygen isotope fractionation between water and the aqueous hydroxide ion. *Geochimica et Cosmochimica Acta*, *289*, 182–195. https://doi.org/10.1016/j.gca.2020.08.025